

Measurement of Charmed Meson Lifetimes

Belle Collaboration

Abstract

The lifetimes of charmed mesons have been measured using 2.75 fb^{-1} of data collected with the Belle detector at KEKB. Each candidate is fully reconstructed to identify the flavor of the charmed meson. The lifetimes are measured to be $\tau(D^0) = (414.8 \pm 3.8 \pm 3.4) \text{ fs}$, $\tau(D^+) = (1040^{+23}_{-22} \pm 18) \text{ fs}$ and $\tau(D_s^+) = (479^{+17+6}_{-16-8}) \text{ fs}$, where the first error is statistical and the second error is systematic. The ratios of the lifetimes of D^+ and D_s^+ with respect to D^0 are measured to be $\tau(D^+)/\tau(D^0) = 2.51 \pm 0.06 \pm 0.04$ and $\tau(D_s^+)/\tau(D^0) = 1.15 \pm 0.04^{+0.01}_{-0.02}$. The mixing parameter y_{CP} is also measured through the lifetime difference of D^0 mesons decaying into CP-mixed states and CP eigenstates. We find $y_{CP} = (1.0^{+3.8+1.1}_{-3.5-2.1}) \%$, corresponding to a 95% confidence interval $-7.0\% < y_{CP} < 8.7\%$. All results are preliminary.

A. Abashian⁴⁴, K. Abe⁸, K. Abe³⁶, I. Adachi⁸, Byoung Sup Ahn¹⁴, H. Aihara³⁷,
 M. Akatsu¹⁹, G. Alimonti⁷, K. Aoki⁸, K. Asai²⁰, M. Asai⁹, Y. Asano⁴², T. Aso⁴¹,
 V. Aulchenko², T. Aushev¹², A. M. Bakich³³, E. Banas¹⁵, S. Behari⁸, P. K. Behera⁴³,
 D. Beil提高², A. Bondar², A. Bozek¹⁵, T. E. Browder⁷, B. C. K. Casey⁷, P. Chang²³,
 Y. Chao²³, B. G. Cheon³², S.-K. Choi⁶, Y. Choi³², Y. Doi⁸, J. Dragic¹⁷, A. Drutskoy¹²,
 S. Eidelman², Y. Enari¹⁹, R. Enomoto^{8,10}, C. W. Everton¹⁷, F. Fang⁷, H. Fujii⁸,
 K. Fujimoto¹⁹, Y. Fujita⁸, C. Fukunaga³⁹, M. Fukushima¹⁰, A. Garmash^{2,8}, A. Gordon¹⁷,
 K. Gotow⁴⁴, H. Guler⁷, R. Guo²¹, J. Haba⁸, T. Haji⁴, H. Hamasaki⁸, K. Hanagaki²⁹,
 F. Handa³⁶, K. Hara²⁷, T. Hara²⁷, T. Haruyama⁸, N. C. Hastings¹⁷, K. Hayashi⁸,
 H. Hayashii²⁰, M. Hazumi²⁷, E. M. Heenan¹⁷, Y. Higashi⁸, Y. Higasino¹⁹, I. Higuchi³⁶,
 T. Higuchi³⁷, T. Hirai³⁸, H. Hirano⁴⁰, M. Hirose¹⁹, T. Hojo²⁷, Y. Hoshi³⁵, K. Hoshina⁴⁰,
 W.-S. Hou²³, S.-C. Hsu²³, H.-C. Huang²³, Y.-C. Huang²¹, S. Ichizawa³⁸, Y. Igarashi⁸,
 T. Iijima⁸, H. Ikeda⁸, K. Ikeda²⁰, K. Inami¹⁹, Y. Inoue²⁶, A. Ishikawa¹⁹, R. Itoh⁸,
 G. Iwai²⁵, M. Iwai⁸, H. Iwasaki⁸, Y. Iwasaki⁸, D. J. Jackson²⁷, P. Jalocha¹⁵, H. K. Jang³¹,
 M. Jones⁷, R. Kagan¹², H. Kakuno³⁸, J. Kaneko³⁸, J. H. Kang⁴⁵, J. S. Kang¹⁴,
 P. Kapusta¹⁵, K. Kasami⁸, N. Katayama⁸, H. Kawai³, M. Kawai⁸, N. Kawamura¹,
 T. Kawasaki²⁵, H. Kichimi⁸, D. W. Kim³², Heejong Kim⁴⁵, H. J. Kim⁴⁵, Hyunwoo Kim¹⁴,
 S. K. Kim³¹, K. Kinoshita⁵, S. Kobayashi³⁰, S. Koike⁸, Y. Kondo⁸, H. Konishi⁴⁰,
 K. Korotushenko²⁹, P. Krokovny², R. Kulasiri⁵, S. Kumar²⁸, T. Kuniya³⁰, E. Kurihara³,
 A. Kuzmin², Y.-J. Kwon⁴⁵, M. H. Lee⁸, S. H. Lee³¹, C. Leonidopoulos²⁹, H.-B. Li¹¹,
 R.-S. Lu²³, Y. Makida⁸, A. Manabe⁸, D. Marlow²⁹, T. Matsubara³⁷, T. Matsuda⁸,
 S. Matsui¹⁹, S. Matsumoto⁴, T. Matsumoto¹⁹, K. Misono¹⁹, K. Miyabayashi²⁰,
 H. Miyake²⁷, H. Miyata²⁵, L. C. Moffitt¹⁷, G. R. Moloney¹⁷, G. F. Moorhead¹⁷,
 N. Morgan⁴⁴, S. Mori⁴², T. Mori⁴, A. Murakami³⁰, T. Nagamine³⁶, Y. Nagasaka¹⁸,
 Y. Nagashima²⁷, T. Nakadaira³⁷, T. Nakamura³⁸, E. Nakano²⁶, M. Nakao⁸, H. Nakazawa⁴,
 J. W. Nam³², S. Narita³⁶, Z. Natkaniec¹⁵, K. Neichi³⁵, S. Nishida¹⁶, O. Nitoh⁴⁰,
 S. Noguchi²⁰, T. Nozaki⁸, S. Ogawa³⁴, R. Ohkubo⁸, T. Ohshima¹⁹, Y. Ohshima³⁸,
 T. Okabe¹⁹, T. Okazaki²⁰, S. Okuno¹³, S. L. Olsen⁷, W. Ostrowicz¹⁵, H. Ozaki⁸,
 P. Pakhlov¹², H. Palka¹⁵, C. S. Park³¹, C. W. Park¹⁴, H. Park¹⁴, L. S. Peak³³, M. Peters⁷,
 L. E. Piilonen⁴⁴, E. Prebys²⁹, J. Raaf⁵, J. L. Rodriguez⁷, N. Root², M. Rozanska¹⁵,
 K. Rybicki¹⁵, J. Ryuko²⁷, H. Sagawa⁸, Y. Sakai⁸, H. Sakamoto¹⁶, H. Sakaue²⁶,
 M. Satapathy⁴³, N. Sato⁸, A. Satpathy^{8,5}, S. Schrenk⁴⁴, S. Semenov¹², Y. Settai⁴,
 M. E. Sevier¹⁷, H. Shibuya³⁴, B. Shwartz², A. Sidorov², V. Sidorov², S. Stanič⁴², A. Sugi¹⁹,
 A. Sugiyama¹⁹, K. Sumisawa²⁷, T. Sumiyoshi⁸, J. Suzuki⁸, J.-I. Suzuki⁸, K. Suzuki³,
 S. Suzuki¹⁹, S. Y. Suzuki⁸, S. K. Swain⁷, H. Tajima³⁷, T. Takahashi²⁶, F. Takasaki⁸,
 M. Takita²⁷, K. Tamai⁸, N. Tamura²⁵, J. Tanaka³⁷, M. Tanaka⁸, Y. Tanaka¹⁸,
 G. N. Taylor¹⁷, Y. Teramoto²⁶, M. Tomoto¹⁹, T. Tomura³⁷, S. N. Tovey¹⁷, K. Trabelsi⁷,
 T. Tsuboyama⁸, Y. Tsujita⁴², T. Tsukamoto⁸, T. Tsukamoto³⁰, S. Uehara⁸, K. Ueno²³,
 N. Ujiie⁸, Y. Unno³, S. Uno⁸, Y. Ushiroda¹⁶, Y. Usov², S. E. Vahsen²⁹, G. Varner⁷,
 K. E. Varvell³³, C. C. Wang²³, C. H. Wang²², M.-Z. Wang²³, T.-J. Wang¹¹, Y. Watanabe³⁸,
 E. Won³¹, B. D. Yabsley⁸, Y. Yamada⁸, M. Yamaga³⁶, A. Yamaguchi³⁶, H. Yamaguchi⁸,
 H. Yamamoto⁷, H. Yamaoka⁸, Y. Yamaoka⁸, Y. Yamashita²⁴, M. Yamauchi⁸, S. Yanaka³⁸,
 M. Yokoyama³⁷, K. Yoshida¹⁹, Y. Yusa³⁶, H. Yuta¹, C.-C. Zhang¹¹, H. W. Zhao⁸,
 Y. Zheng⁷, V. Zhilich², and D. Žontar⁴²

- ¹Aomori University, Aomori
- ²Budker Institute of Nuclear Physics, Novosibirsk
- ³Chiba University, Chiba
- ⁴Chuo University, Tokyo
- ⁵University of Cincinnati, Cincinnati, OH
- ⁶Gyeongsang National University, Chinju
- ⁷University of Hawaii, Honolulu HI
- ⁸High Energy Accelerator Research Organization (KEK), Tsukuba
- ⁹Hiroshima Institute of Technology, Hiroshima
- ¹⁰Institute for Cosmic Ray Research, University of Tokyo, Tokyo
- ¹¹Institute of High Energy Physics, Chinese Academy of Sciences, Beijing
- ¹²Institute for Theoretical and Experimental Physics, Moscow
- ¹³Kanagawa University, Yokohama
- ¹⁴Korea University, Seoul
- ¹⁵H. Niewodniczanski Institute of Nuclear Physics, Krakow
- ¹⁶Kyoto University, Kyoto
- ¹⁷University of Melbourne, Victoria
- ¹⁸Nagasaki Institute of Applied Science, Nagasaki
- ¹⁹Nagoya University, Nagoya
- ²⁰Nara Women's University, Nara
- ²¹National Kaohsiung Normal University, Kaohsiung
- ²²National Lien-Ho Institute of Technology, Miao Li
- ²³National Taiwan University, Taipei
- ²⁴Nihon Dental College, Niigata
- ²⁵Niigata University, Niigata
- ²⁶Osaka City University, Osaka
- ²⁷Osaka University, Osaka
- ²⁸Panjab University, Chandigarh
- ²⁹Princeton University, Princeton NJ
- ³⁰Saga University, Saga
- ³¹Seoul National University, Seoul
- ³²Sungkyunkwan University, Suwon
- ³³University of Sydney, Sydney NSW
- ³⁴Toho University, Funabashi
- ³⁵Tohoku Gakuin University, Tagajo
- ³⁶Tohoku University, Sendai
- ³⁷University of Tokyo, Tokyo
- ³⁸Tokyo Institute of Technology, Tokyo
- ³⁹Tokyo Metropolitan University, Tokyo
- ⁴⁰Tokyo University of Agriculture and Technology, Tokyo
- ⁴¹Toyama National College of Maritime Technology, Toyama
- ⁴²University of Tsukuba, Tsukuba
- ⁴³Utkal University, Bhubaneswer
- ⁴⁴Virginia Polytechnic Institute and State University, Blacksburg VA
- ⁴⁵Yonsei University, Seoul

I. INTRODUCTION

Measurements of individual charmed meson lifetimes provide useful information for the theoretical understanding of the heavy flavor decay mechanisms. In the Heavy Quark Expansion, the decay rate of a heavy flavor hadron is given as [1]

$$\Gamma = \frac{G_F^2 m_Q^5}{192\pi^3} \sum f_i |V_{Qq_i}|^2 [A_1 + \frac{A_2}{m_Q^2} + \frac{A_3}{m_Q^3} + \dots]$$

where f_i is a phase space factor for a given light quark q_i . The A_1 term corresponds to the spectator process, the A_2 term accounts for the difference between the meson and baryon lifetimes, and the A_3 term accounts for W -exchange, W -annihilation and Pauli interference effects. Naively, non-spectator contributions are suppressed by powers of the heavy quark mass and the ratio of charmed meson lifetimes is expected to be close to 1. It is well understood that the large lifetime ratio of D^+ to D^0 , $\tau(D^+)/\tau(D^0) = 2.55 \pm 0.04$ [2-7] is due to destructive interference of the two \bar{d} quarks in the final states of D^+ decays. On the other hand, the ratio of D_s^+ to D^0 lifetimes is expected to lie within the range 1.00–1.07 without W -exchange and W -annihilation effects [8]. However, experimental results[2–7,9] yield $\tau(D_s^+)/\tau(D^0) = 1.191 \pm 0.024$ [10] which is inconsistent with the theoretical expectation. This indicates that the W -exchange contribution is significantly larger than the W -annihilation contribution. It is a theoretical challenge to explain this discrepancy.

Moreover, the $D^0\bar{D}^0$ mixing parameters, $y \equiv (\Gamma_H - \Gamma_L)/(\Gamma_H + \Gamma_L)$ and $x \equiv 2(M_H - M_L)/(\Gamma_H + \Gamma_L)$, can be explored by measuring the lifetime difference of the D^0 meson decaying into a CP-mixed state $D^0 \rightarrow K^-\pi^+$ and a CP-eigenstate $D^0 \rightarrow K^-K^+$. The parameter y_{CP} , defined by

$$y_{CP} \equiv \frac{\Gamma(\text{CP even}) - \Gamma(\text{CP odd})}{\Gamma(\text{CP even}) + \Gamma(\text{CP odd})} = \frac{\tau(D^0 \rightarrow K^-\pi^+)}{\tau(D^0 \rightarrow K^-K^+)} - 1,$$

is related to y and x by the expression

$$y_{CP} = y \cos \phi - \frac{A_{mix}}{2} x \sin \phi,$$

where ϕ is a CP violating weak phase due to the interference of decays with and without mixing, and A_{mix} is related to CP violation in mixing, playing a role similar to $\mathcal{R}e(\epsilon)$ in $K^0\bar{K}^0$ -mixing. E791 [7] and FOCUS [9] have measured $y_{CP} = (0.8 \pm 2.9 \pm 1.0)\%$ and $y_{CP} = (3.42 \pm 1.39 \pm 0.74)\%$ respectively. It is interesting that the FOCUS result is non-zero by more than two standard deviations. On the other hand, CLEO gives results [11] for $D^0\bar{D}^0$ mixing through $D^0 \rightarrow K^+\pi^-$, $y' \cos \phi = (-2.5_{-1.6}^{+1.4})\%$, $x' = (0.0 \pm 1.5 \pm 0.2)\%$ and $A_{mix} = 0.23_{-0.80}^{+0.63}$, where $y' = y \cos \delta - x \sin \delta$ and $x' = x \cos \delta + y \sin \delta$; the parameter δ is the strong phase between the doubly Cabibbo suppressed decay $D^0 \rightarrow K^+\pi^-$ and the Cabibbo allowed decay $\bar{D}^0 \rightarrow K^+\pi^-$ ($\delta = 0$ in the $SU(3)$ limit). The FOCUS and CLEO results could be consistent if there is a large $SU(3)$ breaking effect in $D^0 \rightarrow K^\pm\pi^\mp$ decays [12]. Improvements of the y_{CP} measurement are needed to solve this problem.

In this report, we present measurements of the lifetimes of charmed mesons using the Belle detector at KEKB. D^0 , D^+ and D_s^+ mesons are fully reconstructed via the following decay chains (charge-conjugate modes are implied throughout this paper):

$$\begin{aligned}
& D^0 \rightarrow K^- \pi^+ \text{ (with and without } D^{*+} \rightarrow D^0 \pi^+ \text{ requirement),} \\
& D^0 \rightarrow K^- K^+, \\
& D^+ \rightarrow K^- \pi^+ \pi^+ \text{ (with } D^{*+} \rightarrow D^+ \pi^0 \text{ requirement),} \\
& D^+ \rightarrow \phi \pi^+, \phi \rightarrow K^+ K^-, \\
& D_s^+ \rightarrow \phi \pi^+, \phi \rightarrow K^+ K^-, \\
& D_s^+ \rightarrow \bar{K}^{*0} K^+, \bar{K}^{*0} \rightarrow K^- \pi^+.
\end{aligned}$$

The data sample consists of approximately 2.75 fb^{-1} of e^+e^- collisions near the $\Upsilon(4S)$ resonance.

II. THE BELLE DETECTOR

The Belle detector is designed and constructed primarily to observe and measure CP violation in B decays. Because of the high luminosity of KEKB ($L_{peak} \approx 2 \times 10^{33} \text{ cm}^{-2} \text{ s}^{-1}$) [13], Belle currently accumulates data at a rate of more than 1.5 fb^{-1} per month. This corresponds to 1.6 million $B\bar{B}$ and 2 million $c\bar{c}$ events per month, allowing precise measurements of B and charmed hadron properties. Due to the asymmetric energies of the colliding beams ($3.5 \text{ GeV} \times 8 \text{ GeV}$), the $\Upsilon(4S)$ and its daughter B mesons are produced at $\beta\gamma \approx 0.425$ in the laboratory frame: the difference in B meson decay times may be measured using the difference in decay vertex positions. This key feature of the Belle experiment allows the measurement of CP violation through mixing in neutral B decays, if it occurs.

The Belle detector consists of a silicon vertex detector (SVD), a central drift chamber (CDC), an aerogel Čerenkov counter (ACC), a time of flight (TOF) and trigger scintillation counter (TSC) system, an electromagnetic calorimeter (ECL), and a K_L /muon detector (KLM).

The SVD measures the precise position of decay vertices. It consists of three layers of double-sided silicon strip detectors (DSSD) in a barrel-only design and covers 86% of solid angle. The three layers are at radii of 3.0, 4.5 and 6 cm respectively. Each DSSD consists of 1280 ϕ strips with $25 \mu\text{m}$ pitch, and 640 z strips with $84 \mu\text{m}$ pitch. Impact parameter resolutions are measured as functions of momentum p (GeV/ c) to be $\sigma_{xy} = 21 \oplus 69/(p\beta \sin^{3/2} \theta) \mu\text{m}$ and $\sigma_z = 41 \oplus 48/(p\beta \sin^{5/2} \theta) \mu\text{m}$, where θ is the polar angle with respect to the beam direction. The signal-to-noise ratio ranges from 16 to 40.

Charged tracks are primarily recognized by the CDC; the SVD helps in the recognition of low- p_T tracks. The CDC covers the $17^\circ < \theta < 150^\circ$ angular region (92% of solid angle in the $\Upsilon(4S)$ rest frame), and consists of 50 cylindrical layers of drift cells organized into 11 super-layers (axial or small-angle-stereo) each containing between three and six layers. He-C₂H₆ (50/50%) gas is used to minimize multiple-Coulomb scattering. The inner and outer radii of the CDC are 9 cm and 86 cm respectively. The magnetic field of 1.5 Tesla is chosen to optimize momentum resolution without sacrificing efficiency for low momentum tracks. The resulting momentum resolution is measured to be 1.1% for 3–5 GeV/ c tracks.

The CDC, TOF and ACC provide K/π separation up to 3.5 GeV/ c . The CDC measures dE/dx and provides 3σ K/π separation and 4σ e/π separation below 0.8 GeV/ c . The TOF system provides 3σ K/π separation up to 1.2 GeV/ c with a TOF time resolution of 100 ps. The aerogel Čerenkov counter (ACC) system extends the coverage for particle identification

upward from the 1.2 GeV/ c limit of the TOF system to the kinematic limit of two-body B decays, *i.e.*, to 2.5–3.5 GeV/ c depending on polar angle. The combination of these particle identification devices is a key feature of the Belle detector. The combinatorial background for D decays is greatly reduced by this powerful kaon identification capability: this is the main reason that we can obtain the lifetime of D^0 without the $D^{*+} \rightarrow D^0\pi^+$ requirement.

The CDC and ECL are used to identify electrons. The ECL also detects photons and measures their energy. The Cesium Iodide (CsI) electromagnetic calorimeter (ECL) consists of 6624 barrel crystals, 1152 forward endcap crystals and 960 backward endcap crystals. All the crystals are 30 cm ($16.1X_0$) long. The energy resolution is measured to be $\sigma_E/E = 2.0\%$ for 4–8 GeV/ c electrons using Bhabha events.

The KLM is designed to detect K_L 's and muons. In particular, detection of the K_L from the $B \rightarrow \psi K_L$ decay is important since it yields a sensitivity to the CP asymmetry which is similar to that of the $B \rightarrow \psi K_S$ decay. The KLM is a repetition of 14 or 15 modules which consist of 47 mm thick iron plates and 44 mm thick slots instrumented with resistive plate counters (RPC).

In Monte Carlo simulation, the physics properties of an event are generated by the QQ event generator developed by the CLEO group. Detector response is simulated by the CERN GEANT package.

A detailed description of the Belle detector can be found elsewhere [14].

III. D RECONSTRUCTION

This section describes the criteria used to select charged tracks, leptons and photons, and the ways in which they are combined to form the mesons used in this analysis.

A. Track selection

All charged tracks must be associated with at least two SVD hits in both the $r\phi$ and rz planes. The SVD hit association efficiency is better than 98% per track. The $\chi^2/N.D.F.$ of the track fit must be less than 10, to reduce badly reconstructed tracks. Charged pion and kaon candidates are required to pass cuts in particle identification likelihood functions based on drift chamber energy deposition, time-of-flight and aerogel Čerenkov counter response. No particle identification is required for the soft pion from the D^{*+} decay.

B. Photon selection

Photon candidates are associated with isolated CsI calorimeter clusters that are not matched to any charged track. A minimum energy cut of 20 MeV is applied.

C. Light meson selection

Decay modes of the light mesons used in this analysis are summarized in Table I. The mass cuts used to select them are also shown.

TABLE I. Decay modes and mass cuts used to select the light mesons.

Mode	Mass cut (MeV/ c^2)
$\pi^0 \rightarrow \gamma\gamma$	$ M_{\gamma\gamma} - M_{\pi^0} < 16.2$
$\phi \rightarrow K^+K^-$	$ M_{K^+K^-} - M_\phi < 6$
$\overline{K}^{*0} \rightarrow K^-\pi^+$	$ M_{K^-\pi^+} - M_{\overline{K}^{*0}} < 50$

A π^0 candidate must contain at least one photon with $-0.63 < \cos\theta_\gamma < 0.84$ (barrel region), where θ_γ is the polar angle with respect to the opposite of the electron beam direction; it must also satisfy the cut $|\cos\theta_D| < 0.9$, where θ_D is the angle between the π^0 candidate and one of the daughter photons, evaluated in the π^0 rest frame. Each photon candidate is included in at most one π^0 candidate. A mass-constrained fit is performed to improve the π^0 momentum resolution.

D. D selection

The $D^0 \rightarrow K^-\pi^+$ (with or without $D^{*+} \rightarrow D^0\pi^+$ requirement), $D^0 \rightarrow K^-K^+$, $D^+ \rightarrow K^-\pi^+\pi^+$ (with $D^{*+} \rightarrow D^+\pi^0$ requirement), $D^+ \rightarrow \phi\pi^+$, $D_s^+ \rightarrow \phi\pi^+$ and $D_s^+ \rightarrow \overline{K}^{*0}K^+$ modes are used to reconstruct charmed meson candidates. The $\chi^2/N.D.F.$ of the vertex-constrained fit for a candidate meson is required to be better than 3 for the D^0 analysis, 4 for the D^+ analysis, and 6 for the D_s^+ analysis. This cut, which rejects many badly-measured events, is important: if too loose a criterion is used, the fraction of badly-measured events becomes large, and modeling of the resolution becomes difficult. The efficiencies of the chosen cuts range from 76–88%.

In two-body D decay modes, a decay angle cut is imposed: $-0.75 < \cos\theta_D$ for $D^0 \rightarrow K^-\pi^+$ and $-0.85 < \cos\theta_D$ for $D_s^+ \rightarrow \phi\pi^+$; no cut is used for $D^0 \rightarrow K^-K^+$. For signal events the $\cos\theta_D$ distribution is flat, while the background from random pions is peaked toward $\cos\theta_D = -1$ (or $\cos\theta_D = 1$, depending on which daughter we choose). In the $\phi\pi^+$ decays a cut $|\cos\theta_H| > 0.4$ is imposed on the helicity angle θ_H , *i.e.* the angle between either of the kaon daughters and the D direction, evaluated in the ϕ rest frame. (In a $P \rightarrow PV$ decay the vector meson is polarized, decaying to two pseudoscalars $V \rightarrow PP$ according to a $\cos^2\theta_H$ distribution; the combinatorial background is flat in $\cos\theta_H$.) The D momentum in the $\Upsilon(4S)$ rest frame is required to be greater than 2.5 GeV/ c^2 to eliminate $B\overline{B}$ events. When multiple candidates share tracks with different particle ID, the candidate with the best kaon ID is retained.

Figs 1, 2 and 3 show the D^0 , D^+ and D_s^+ mass distributions after all selection criteria are applied. Points with error bars indicate data, while the solid curve indicates the fit result. The signal is represented by a sum of two Gaussians while background is represented by a linear function; the background function is indicated by the dotted line in the figure. We find 19304 ± 186 $D^0 \rightarrow K^-\pi^+$ without $D^{*+} \rightarrow D^0\pi^+$ requirements, 1827 ± 58 $D^0 \rightarrow K^-K^+$, 310 ± 21 $D^+ \rightarrow \phi\pi^+$, 1008 ± 33 $D_s^+ \rightarrow \phi\pi^+$ and 580 ± 29 $D_s^+ \rightarrow \overline{K}^{*0}K^+$ signals within 3σ of the measured mean value.

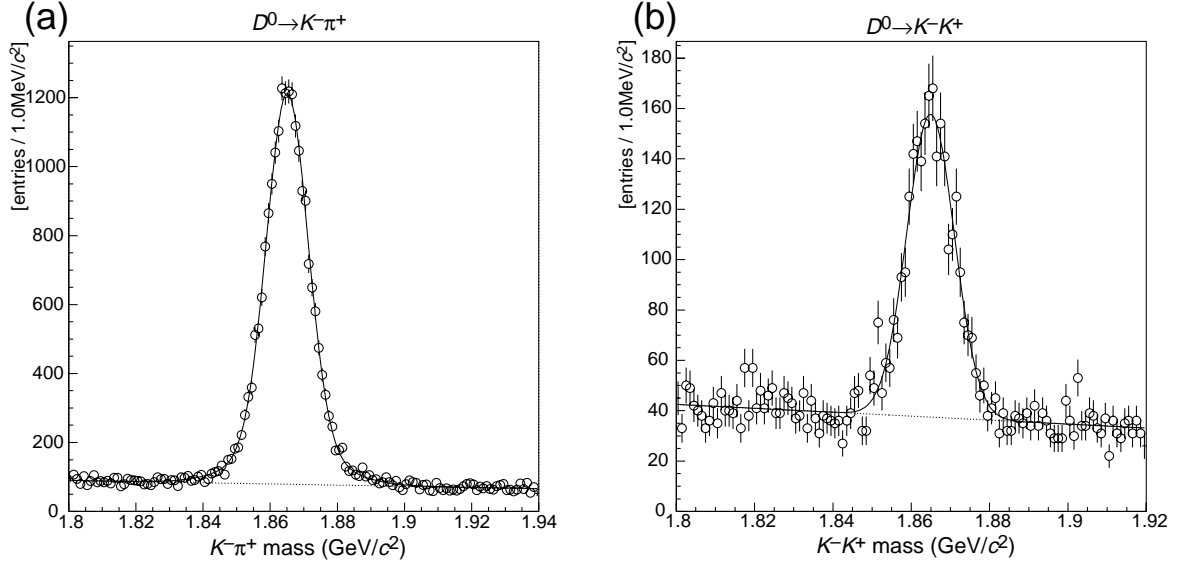


FIG. 1. The D^0 mass distribution for (a) $D^0 \rightarrow K^- \pi^+$ and (b) $D^0 \rightarrow K^- K^+$ candidates. The points with error bars are data while the solid curve indicates the fit result. The signal is represented by a sum of two Gaussians for $D^0 \rightarrow K^- \pi^+$ and a Gaussian for $D^0 \rightarrow K^- K^+$, while the background is represented by a linear function. The background function is indicated by the dotted line.

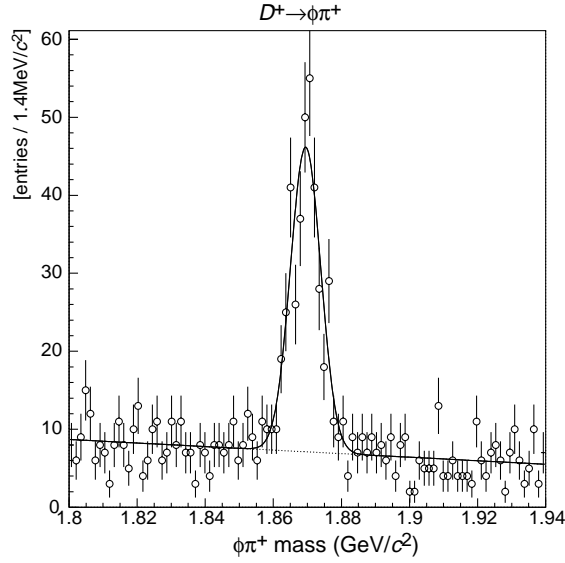


FIG. 2. The D^+ mass distribution for $D^+ \rightarrow \phi \pi^+$ candidates. The points with error bars are data while the solid curve indicates the fit result. The signal is represented by a Gaussian while the background is represented by a linear function. The background function is indicated by the dotted line.

E. D^* selection

The $D^{*+} \rightarrow D\pi$ decay requirement is imposed to reduce the background. D^{*+} candidates are formed by combining D^0 or D^+ candidates with soft pions. The combinations must satisfy the requirement that the mass-difference, $\Delta M = M_{D\pi} - M_D$, be within 3σ of the measured mean value. The typical standard deviations are approximately $0.23 \text{ MeV}/c^2$ for D^0 , and $0.76 \text{ MeV}/c^2$ for the D^+ modes. The ΔM resolution is greatly improved by refitting the soft π^+ track with the constraint that it originates from the D^0 production point, as described in the following section. Figs 4 and 5 show (a) the ΔM distribution for D^* candidates and (b) the D -mass distribution after the ΔM cut. The signal is represented by a sum of two Gaussians while the background is represented by a phase-space function: $(x-x_0)^p e^{a-b(x-x_0)}$ for the ΔM distribution, and a linear function for the D -mass distribution. We find $4160 \pm 69 \text{ } D^0 \rightarrow K^-\pi^+$ and $2021 \pm 49 \text{ } D^+ \rightarrow K^-\pi^+\pi^+$ fulfilling the $D^* \rightarrow D\pi$ requirement.

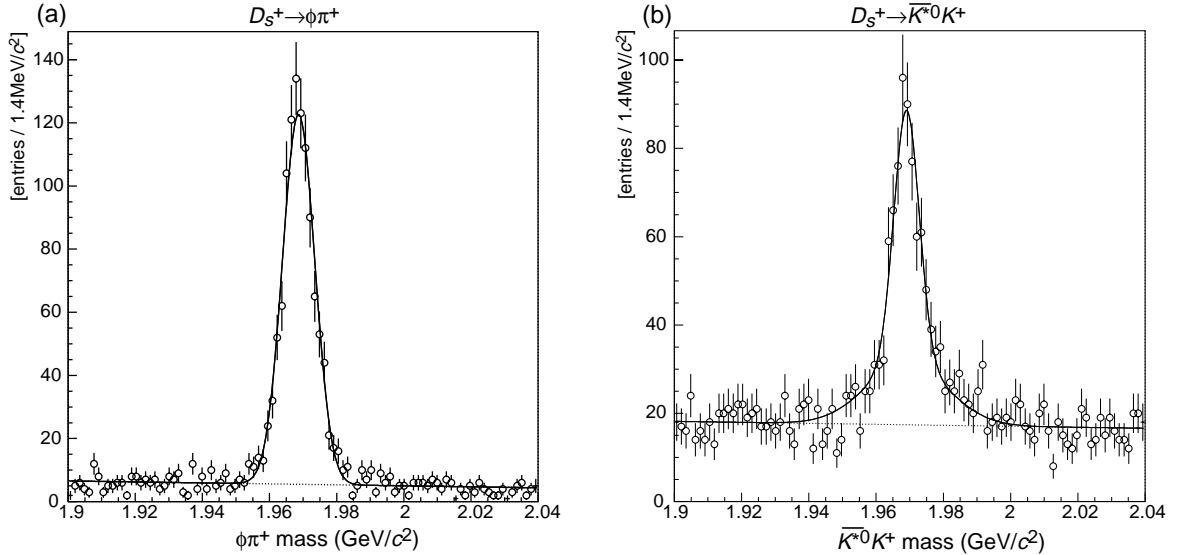


FIG. 3. The D_s^+ mass distribution for (a) $D_s^+ \rightarrow \phi\pi^+$ and (b) $D_s^+ \rightarrow \bar{K}^{*0}K^+$ candidates. The points with error bars are data while the solid curve indicates the fit result. The signal is represented by a Gaussian for $D_s^+ \rightarrow \phi\pi^+$, and a sum of two Gaussians for $D_s^+ \rightarrow \bar{K}^{*0}K^+$. The background is represented by a linear function in each case; its contribution to the fit is shown by the dotted line.

IV. DECAY LENGTH RECONSTRUCTION

The charmed meson lifetime is measured using the distance between the decay and production vertices of the reconstructed charmed mesons.

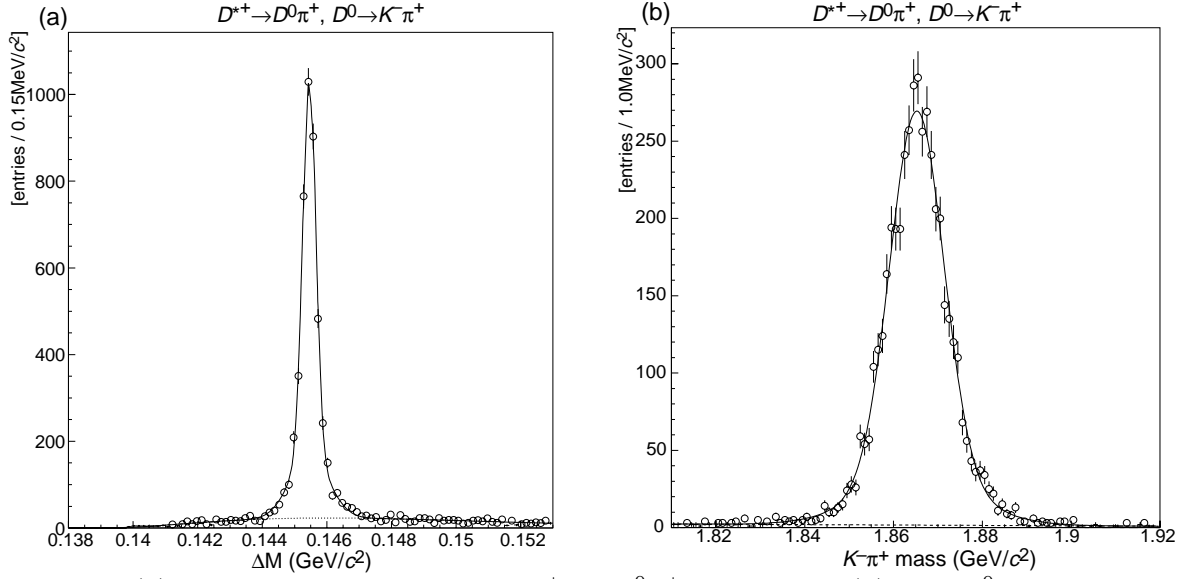


FIG. 4. (a) The ΔM distribution for $D^{*+} \rightarrow D^0\pi^+$ candidates. (b) The D^0 mass distribution after the 3σ ΔM cut. The points with error bars are data while the solid curve indicates the fit result; the background function is shown by the dotted curve. In each case the signal is represented by a sum of two Gaussians while the background is represented by a phase-space function: $(x - x_0)^p e^{a-b(x-x_0)}$ for the ΔM distribution, and a linear function for the D^0 mass distribution.

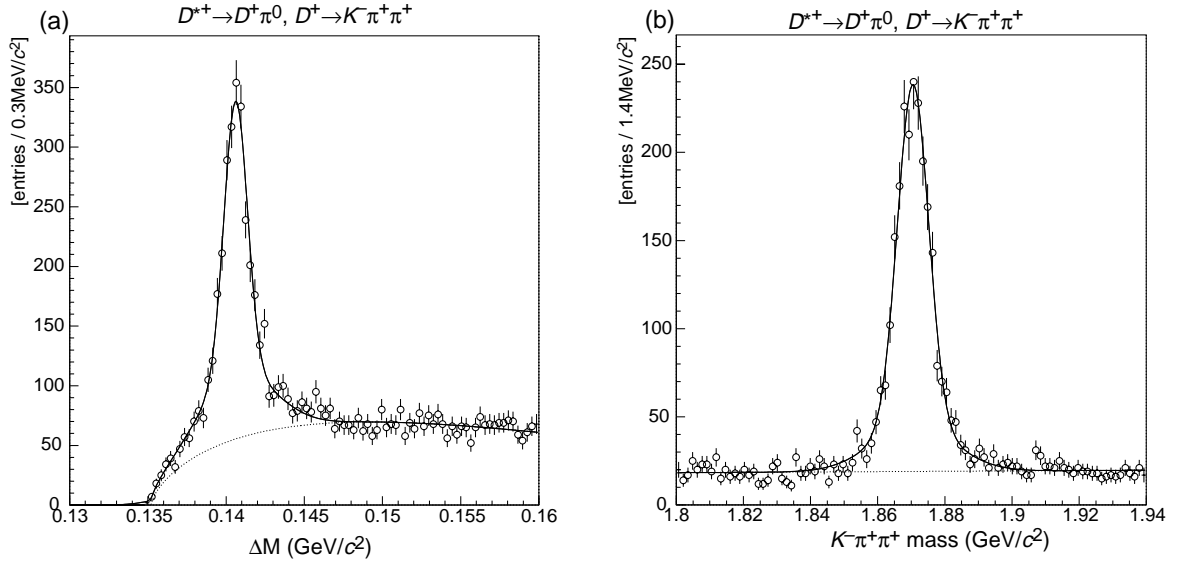


FIG. 5. (a) The ΔM distribution for $D^{*+} \rightarrow D^+\pi^0$ candidates. (b) The D^+ mass distribution after the 3σ ΔM cut. The points with error bars are data while the solid curve indicates the fit result; the background function is shown by the dotted curve. In each case the signal is represented by a sum of two Gaussians while background is represented by a phase-space function: $(x - x_0)^p e^{a-b(x-x_0)}$ for the ΔM distribution, and a linear function for the D^+ mass distribution.

The decay vertex of the reconstructed charmed meson is obtained using all tracks that form the candidate. The typical D decay vertex resolution is approximately $50 \mu\text{m}$.

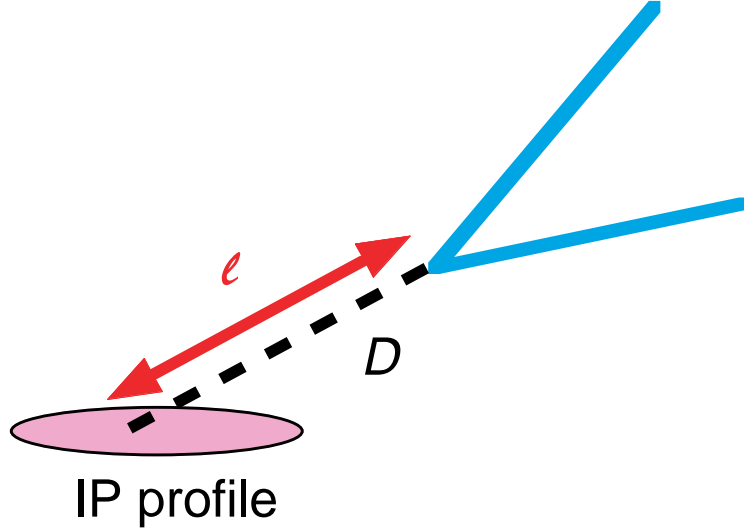


FIG. 6. Illustration for reconstruction of decay and production vertex points of a D meson.

The production vertex is obtained by extrapolating the D flight path to the interaction region. Fig 6 illustrates the reconstruction of the decay and production vertex points of the charmed meson. The $\chi^2/N.D.F.$ of the fit is required to be less than 10 for the D^0 analysis, to reduce badly reconstructed candidates. The soft pion track is not used in the fit for the $D^{*+} \rightarrow D^0\pi^+$ analysis: instead, it is refit with the constraint that it originates from the obtained D^0 production vertex. The average position of the interaction point is calculated offline for every accelerator fill from the primary vertex position distribution of hadronic events. The size of the interaction region in the horizontal direction (x) is calculated using the primary vertex position distribution; the effect of the primary vertex resolution is deconvoluted in this calculation. The vertex resolution is obtained using the primary vertex position distribution in the vertical direction (y), since the beam size in this direction is less than $10 \mu\text{m}$ and the σ of the y direction is a good representation of the vertex resolution. The size of the interaction region in the y direction is determined from the average luminosity, the beam current and the x size of the interaction region. The size of the interaction region is typically $100 \mu\text{m}$ in x and $5 \mu\text{m}$ in y. The vertex resolution of the charmed meson production point is approximately $30 \mu\text{m}$ in x, $5 \mu\text{m}$ in y and $45 \mu\text{m}$ in z for each event. The calculated error of the flight length is typically $90 \mu\text{m}$ and the candidate is rejected if this error is more than $300 \mu\text{m}$.

The proper-time of each D candidate is calculated as

$$t = \frac{\ell \cdot m(D)}{p(D) \cdot c}$$

where ℓ is the flight length of the D . For D^+ and D_s^+ candidates, the helical flight path is properly taken into account, although the effect is small.

V. BACKGROUNDS

Background contributions can be divided into four categories according to the origin of the tracks: those candidates that consist of tracks from the primary vertex, those that consist of tracks from a different origin, those that consist of charm daughters, and those that originate from $B\bar{B}$ events. The first source is the dominant contributor to the background (82% for two-body decays and 60% for three-body decays). It should appear to have zero-lifetime, and the proper-time resolution is expected to be similar to the resolution for the signal. The second source accounts for 17% of the background for two-body decays and 40% for three-body decays. This source appears to have a very short lifetime because of the vertex constraint, and the proper-time resolution is worse than the signal resolution due to the incorrect assignment of the vertex and momentum. The contribution of the third source is very small (less than 1% of backgrounds for both two-body decays and three-body decays) and it should appear to have the lifetime of the parent charmed hadron. The proper-time resolution should be similar to the resolution for the signal. The contribution of the last source is small ($\sim 3\%$). The proper-time distribution of this background is similar to that of the second source.

VI. LIFETIME FIT

An unbinned maximum likelihood fit is performed to extract the charmed meson lifetime. The probability density function is defined as

$$\begin{aligned} P(t) = & f_{SIG} \int_0^\infty dt' \frac{1}{\tau_{SIG}} e^{-t'/\tau_{SIG}} R_{SIG}(t - t') \\ & + (1 - f_{SIG}) f_{\tau BG} \int_0^\infty dt' \frac{1}{\tau_{BG}} e^{-t'/\tau_{BG}} R_{BG}(t - t') \\ & + (1 - f_{SIG})(1 - f_{\tau BG}) \int_0^\infty dt' \delta(t') R'_{BG}(t - t'), \end{aligned}$$

where f_{SIG} and $f_{\tau BG}$ are fractions for the signal and the background with lifetime, τ_{SIG} and τ_{BG} are the signal and background lifetimes, and R_{SIG} and R_{BG} are the resolution functions for the signal and the background.

The fraction f_{SIG} is calculated based on the D mass for each event, using a functional form $f_{SIG}(M_D)$ derived from the data. The D -mass distribution is fit with a Gaussian or a sum of two Gaussians for the D signal and a linear function for the background, and $f_{SIG}(M_D)$ is then defined as

$$f_{SIG}(M_D) = \frac{F_{SIG}(M_D)}{F_{BG}(M_D) + F_{SIG}(M_D)}$$

where F_{SIG} and F_{BG} are the D signal and background functions described above.

A large D -mass sideband region ($-60 \text{ MeV}/c^2 \sim -3\sigma$ and $+3\sigma \sim +70 \text{ MeV}/c^2$ for D^0 , $\pm 3\sigma \sim \pm 50 \text{ MeV}/c^2$ for D^+ and D_s^+) is used to determine the fit parameters for the background. The lifetime fit is made for the D -mass signal (within 3σ) and sideband regions simultaneously.

A. Resolution Function

The parameterization of the resolution function will now be discussed. Fig 7 shows the distribution of $t_{rec} - t_{gen}$ obtained from MC data, where t_{rec} is the reconstructed proper-time of the candidate and t_{gen} is the true proper-time. A fit to a sum of two Gaussians is also shown. The fit is not a good representation of the distribution since the vertex resolution depends on track momenta, angles and other factors, and therefore the distribution consists of many Gaussians. We can calculate the track error event by event using a Kalman filtering technique that takes into account the resolution of each hit, multiple scattering and energy loss. Fig 8 shows the distribution of $(t_{rec} - t_{gen})/\sigma_t$ where σ_t is the calculated proper-time error for each event. The distribution is well-represented by a fit to a sum of two Gaussians, shown in the figure by the overlaid solid curve. The standard deviation of the main Gaussian would be 1.0 if the error estimation were correct, whereas the fitted value is 1.1: the difference is considered to be due to underestimation of the tracking error. The remaining events, represented by the second, broader Gaussian, are considered to be badly measured, due to mis-association of SVD hits, incorrect SVD-hit clustering, hard scattering of tracks and so on.

Based on the success of this fit, we represent the proper-time resolution using the function:

$$R_{SIG}(x) = (1 - f_{tail}) \cdot G(x; S\sigma_t) + f_{tail} \cdot G(x; S_{tail}\sigma_t),$$

$$G(x; \sigma) \equiv \frac{1}{\sqrt{2\pi}\sigma} e^{-\frac{x^2}{2\sigma^2}},$$

where S and S_{tail} are global scaling factors for the estimated error σ_t for the main and tail Gaussian distributions, and f_{tail} is the fraction of the tail part.

Fig 9 shows the σ_t distribution for MC signal events. A small fraction of events have a large σ_t . We evaluate the effect of these large σ_t events on the resolution function by dividing the signal events into three samples according to σ_t , one sample with $\sigma_t < 120$ fs (lower side of the peak), another sample with $120 < \sigma_t < 400$ fs (higher side of the peak) and a third sample with $400 < \sigma_t$ (the tail). We fit the $t_{rec} - t_{gen}$ distributions with resolution functions for these three samples as shown in Fig 10. Table II lists the fit results: the parameter estimates in the three σ_t regions are comparable, although a trend is evident, especially in the parameters of the tail.

TABLE II. Fit parameters from fits to $t_{rec} - t_{gen}$ distributions with the resolution function.

σ_t region (fs)	S	S_{tail}	f_{tail}
$\sigma_t < 120$	1.19 ± 0.01	3.56 ± 0.09	0.031 ± 0.002
$120 < \sigma_t < 400$	1.15 ± 0.01	3.12 ± 0.08	0.043 ± 0.004
$400 < \sigma_t$	1.12 ± 0.01	2.96 ± 0.17	0.050 ± 0.010
all	1.18 ± 0.01	3.41 ± 0.05	0.035 ± 0.002

In the analysis presented here we use the same functional form for the resolution function, regardless of the σ_t value. The effect of ignoring the small σ_t dependence of the resolution

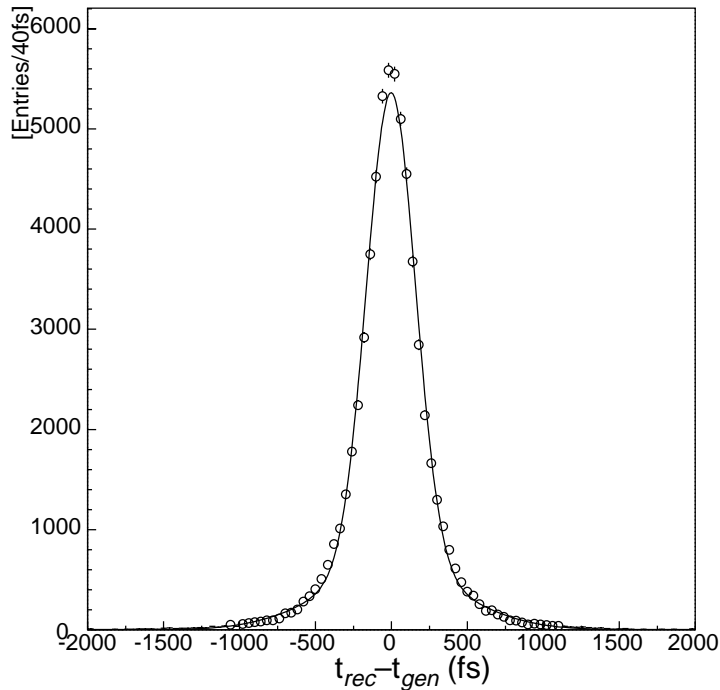


FIG. 7. The distribution of $t_{rec} - t_{gen}$ in the MC data

function parameters has been assessed by performing a lifetime fit for signal events in the Monte Carlo, using only the signal part of the probability density function. Table III shows the results: the fit yields a lifetime 412.5 ± 1.4 fs, which is consistent with the true lifetime of the Monte Carlo sample, 412.6 fs. (The parameters of the resolution function given by this lifetime fit are consistent with the parameters shown in Table II.) We conclude that the σ_t dependence of the resolution function parameters does not significantly affect the lifetime fit.

TABLE III. Results from a lifetime fit to the proper-time distribution of MC signal events.

Fit parameter	Fit values
τ_{SIG}	412.5 ± 1.4
S	1.19 ± 0.01
S_{tail}	3.55 ± 0.05
f_{tail}	0.028 ± 0.003

B. Background function

The proper-time distribution for the background is represented by two components: one with lifetime, and one without. This distribution is then convoluted with a resolution

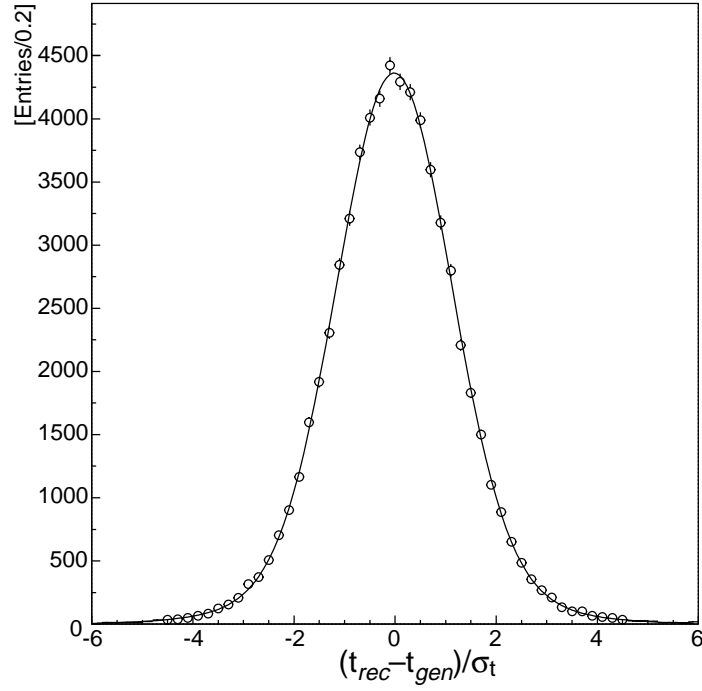


FIG. 8. The distribution of $(t_{rec} - t_{gen})/\sigma_t$ in the MC data: a fit to a sum of two Gaussians is superimposed.

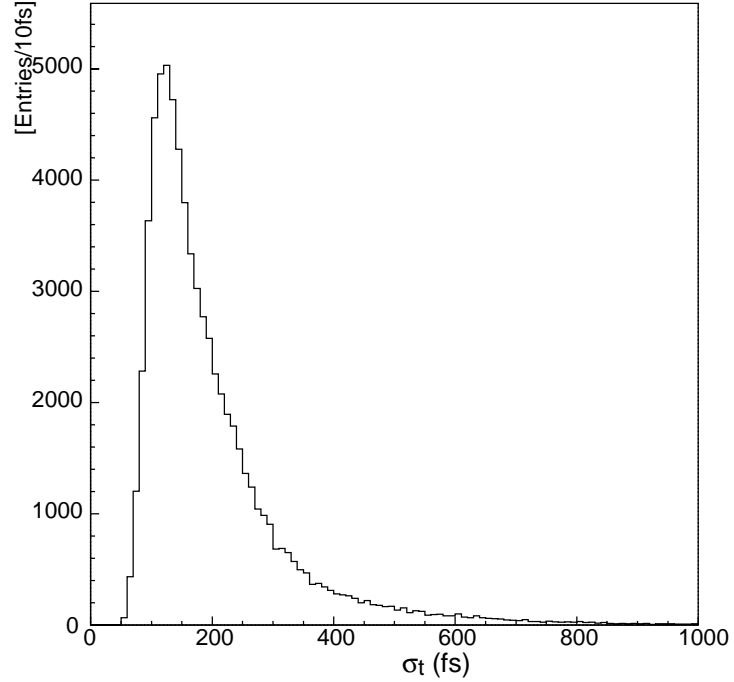


FIG. 9. The σ_t distribution for signal events. A small fraction of events have large σ_t .

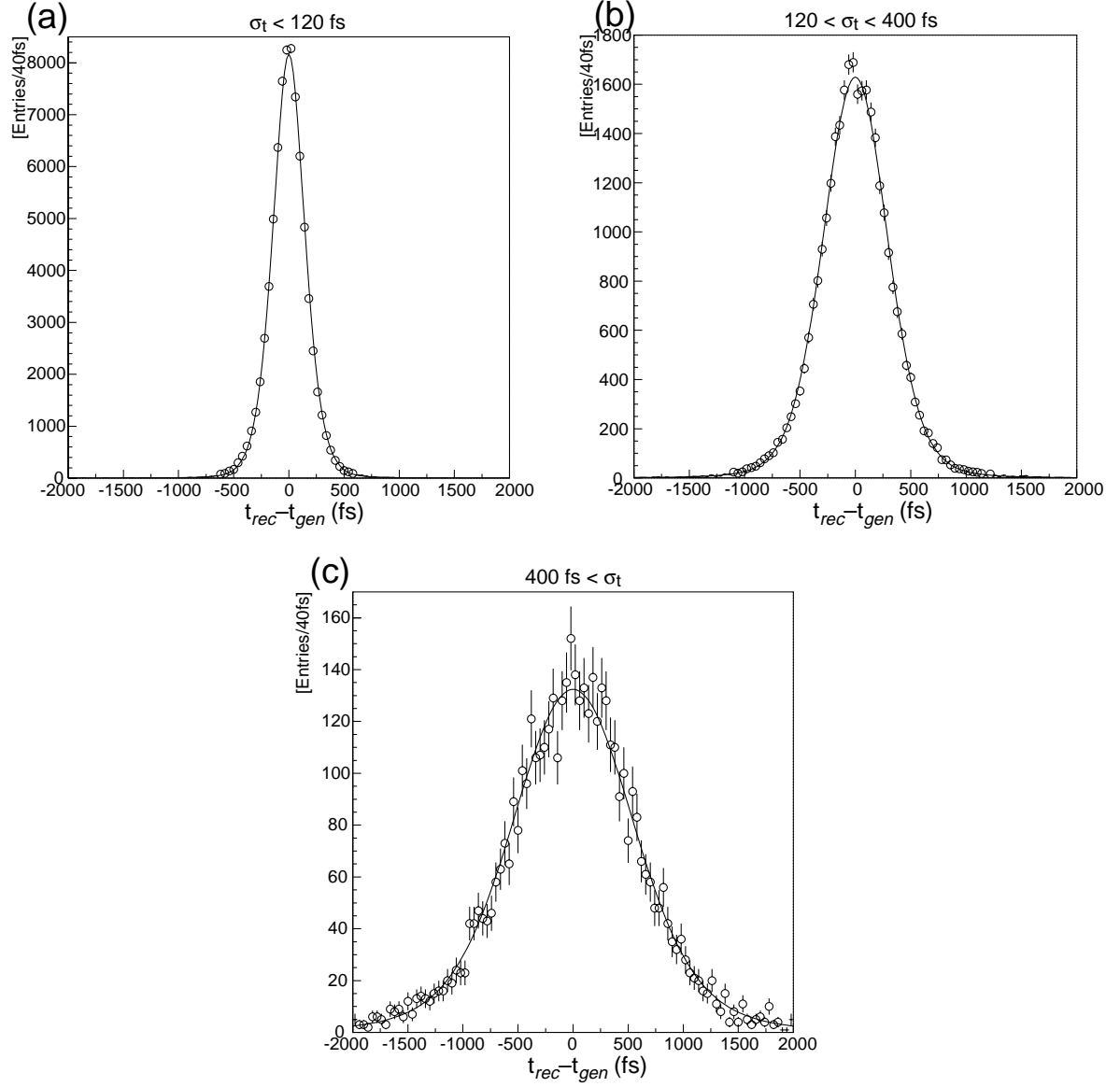


FIG. 10. Fits of the resolution function to $t_{rec} - t_{gen}$ distributions in the (a) lower, (b) higher and (c) tail regions of the σ_t distribution, for MC signal events.

function: the functional form is the same as that used for the signal, but the parameters are fitted independently, as wrong combinations are likely to be used to form the D candidates in the background. In principle, the resolution function could be different for the two background components, but we cannot separately determine the resolution function for the background with lifetime, due to limited statistics: therefore a single resolution function is used,

$$R_{BG}(x) = (1 - f_{tail}^{BG}) \cdot G(x; S_{BG}\sigma_t) + f_{tail}^{BG} \cdot G(x; S_{tail}^{BG}\sigma_t).$$

Fig 11 compares proper-time distributions of backgrounds under the D peak with those in the sideband for (a),(b) $D^0 \rightarrow K^-\pi^+$ and (c),(d) $D_s^+ \rightarrow \phi\pi^+$. Table IV then compares fit parameters between the D -mass signal and sideband regions: the results in the two regions are similar, which supports the D -mass independence of the proper-time. The scaling factor for the tail (S_{tail}^{BG}) and the tail fraction (f_{tail}^{BG}) are comparable to those of the signal resolution function (S_{tail} and f_{tail}). Using the S_{tail} and f_{tail} values in Table III, and $S_{tail}^{BG} = 3.19 \pm 0.15$ and $f_{tail}^{BG} = 0.054 \pm 0.007$ obtained by combining the background samples in the signal and sideband regions, we fix the ratios $S_{tail}^{BG}/S_{tail} = 0.90 \pm 0.06$ and $f_{tail}^{BG}/f_{tail} = 1.9 \pm 0.4$ in the lifetime fit, in order to minimize the number of fit parameters. We evaluate systematic errors associated with this constraint by changing these ratios by $\pm 2\sigma$.

The background shape obtained in the $D^0 \rightarrow K^-\pi^+$ analysis is used for the $D^{*+} \rightarrow D^0\pi^+$, $D^0 \rightarrow K^-\pi^+$ analysis since we do not have enough statistics for the background shape determination with the D^* requirement.

TABLE IV. Comparisons of fit parameters for background proper-time distributions between the D -mass signal and sideband regions.

Fit parameters	$D^0 \rightarrow K^-\pi^+$		$D_s^+ \rightarrow \phi\pi^+$	
	D signal	D sideband	D signal	D sideband
τ_{BG}	423 ± 54	368 ± 35	467 ± 221	467 ± 161
$f_{\tau BG}$	0.05 ± 0.01	0.05 ± 0.01	0.07 ± 0.04	0.03 ± 0.02
S_{BG}	1.22 ± 0.02	1.20 ± 0.01	1.27 ± 0.07	1.28 ± 0.05
S_{tail}^{BG}	3.81 ± 0.29	3.01 ± 0.13	4.2 ± 1.3	2.9 ± 0.5
f_{tail}^{BG}	0.04 ± 0.01	0.06 ± 0.01	0.05 ± 0.04	0.07 ± 0.04

C. Fit results

Using the probability density function described above, the likelihood function has the form:

$$\begin{aligned}
& L(\tau_{SIG}, \tau_{BG}, f_{\tau BG}, S, S_{tail}, f_{tail}, S_{BG}) \\
&= \prod_i \int_0^\infty dt' [f_{SIG}^i \frac{1}{\tau_{SIG}} e^{-t'/\tau_{SIG}} R_{SIG}(t_i - t') \\
&\quad + (1 - f_{SIG}^i) \{f_{\tau BG} \frac{1}{\tau_{BG}} e^{-t'/\tau_{BG}} + (1 - f_{\tau BG})\delta(t')\} R_{BG}(t_i - t')],
\end{aligned}$$

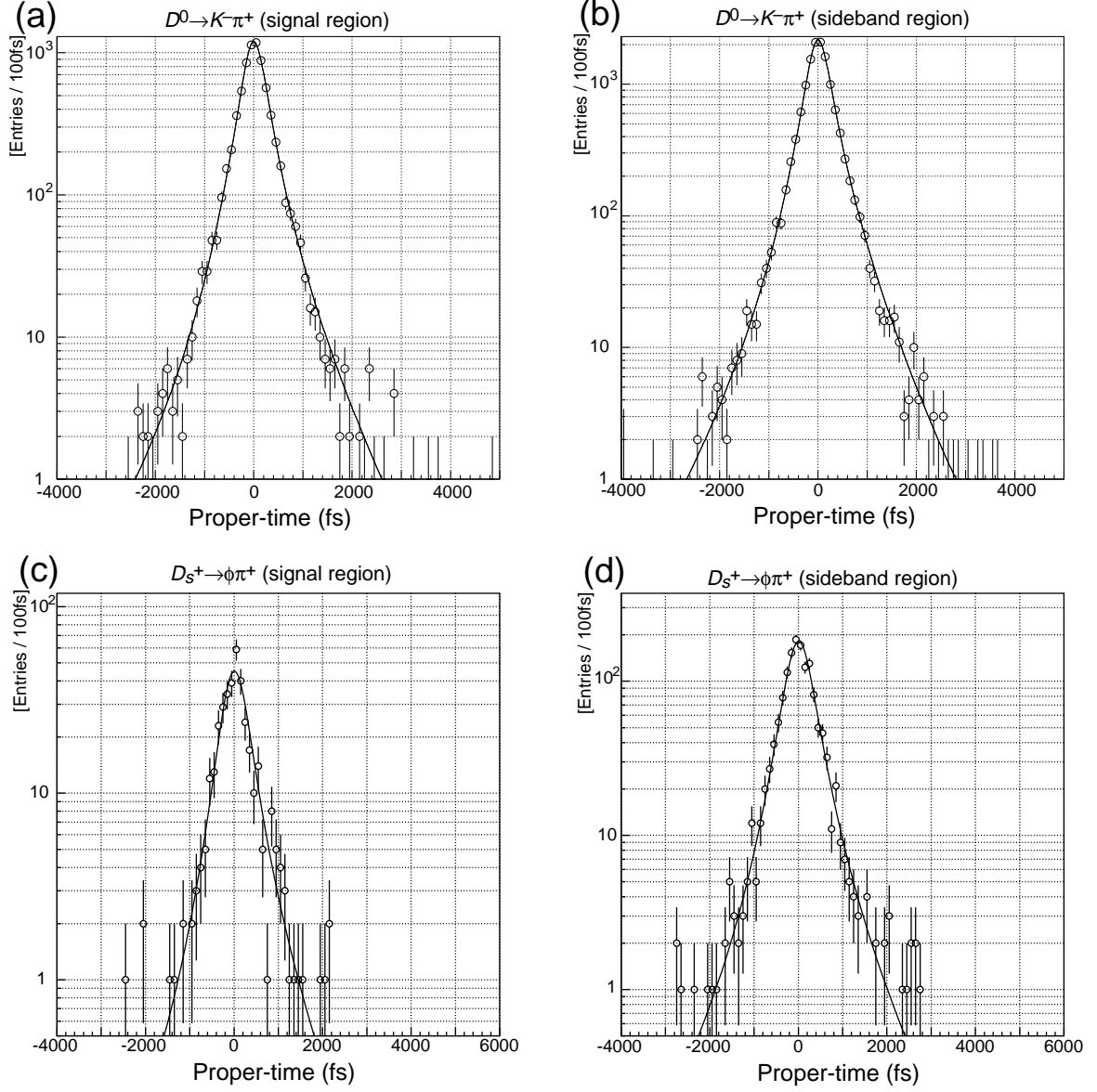


FIG. 11. A comparison of proper-time distributions in MC data for backgrounds under the D peak (within 3σ) and those in the sideband ($-60 \text{ MeV}/c^2 \sim -3\sigma$, $3\sigma \sim 70 \text{ MeV}/c^2$ for D^0 , $\pm 3\sigma \sim \pm 50 \text{ MeV}/c^2$ for D^+ and D_s^+) for (a),(b) $D^0 \rightarrow K^- \pi^+$ and (c),(d) $D_s^+ \rightarrow \phi \pi^+$. Fit results are superimposed.

$$\begin{aligned}
R_{SIG}(x) &= (1 - f_{tail}) \cdot G(x; S\sigma_t^i) + f_{tail} \cdot G(x; S_{tail}\sigma_t^i), \\
R_{BG}(x) &= (1 - f_{tail}^{BG}) \cdot G(x; S_{BG}\sigma_t^i) + f_{tail}^{BG} \cdot G(x; S_{tail}^{BG}\sigma_t^i),
\end{aligned}$$

where τ_{SIG} , τ_{BG} , $f_{\tau BG}$, S , S_{tail} , f_{tail} and S_{BG} are allowed to float. The ratios S_{tail}^{BG}/S_{tail} and f_{tail}^{BG}/f_{tail} are fixed at values obtained from the MC simulation for each decay mode. We reject candidates with proper-time greater than 5 ps for the D^0 analysis and 6 ps for the D_s^+ analysis.

Figs 12, 13, 14 and 15 show the lifetime fit results for D^0 decays without the D^{*+} requirement, $D^+ \rightarrow \phi\pi^+$ decay, D_s^+ decays, and D^0 and D^+ decays with the D^* requirement. In each figure, (a) and (c) show the results in the D -mass signal region while (b) and (d) show the results in the D -mass sideband region. The solid lines show the fit and the dotted lines show the background contribution in the fit. Tables V (a)–(c) summarize the fit parameters obtained from the lifetime fit.

Figs 16(a) to (g) show the log-likelihood as a function of τ_{SIG} for all decay modes: they have parabolic shape as expected. The goodness of fit is further evaluated by performing many “toy Monte Carlo experiments”. For each mode, one hundred sets of MC data with the same statistics as the data are generated with the probability density function obtained from the lifetime fit. Figs 17(a) to (g) show the distributions of log-likelihood from the toy Monte Carlo data sets in each of the decay modes. Table VI summarizes the confidence levels of the fits derived from these distributions: the confidence levels are found to be reasonable.

VII. SYSTEMATIC UNCERTAINTIES

We consider systematic effects from the reconstruction of the D decay length, and from the fit function in the following subsections. The major contributions to the systematic error are found to be the uncertainties in the t dependence of the reconstruction efficiency, the understanding of the resolution tail, and the decay length reconstruction; the results are summarized in Tables VII (a)–(c). All systematic errors are combined in quadrature.

A. Systematic error due to reconstruction

- **IP size and position dependence:** The size and average position of the IP is measured for each accelerator fill; the resulting error of the IP position is $1.4 \mu\text{m}$ in x and $0.9 \mu\text{m}$ in y . These errors are included in the IP-constrained fit. We vary the IP position by $5 \mu\text{m}$ in x and $3 \mu\text{m}$ in y and repeat the analysis. The IP size has an uncertainty of $5 \mu\text{m}$ in x and $2 \mu\text{m}$ in y : we vary the IP size by these amounts and repeat the analysis. We observe a very small effect on the lifetime.
- **t dependence of reconstruction efficiency:** The t dependence of the reconstruction efficiency has been studied in the Monte Carlo data: Fig 18 shows the reconstruction efficiencies as functions of the proper-time t for the major modes. In each case, a χ^2 fit to a linear function $\epsilon_0(1 + \alpha t)$ is made to find the slope; the parameter ϵ_0 is the

TABLE V. Summary of fit parameters obtained from the lifetime fit.

(a) Fit parameters for the D^0 decay modes.

Fit parameters	$D^0 \rightarrow K^- \pi^+$	$D^0 \rightarrow K^- K^+$	$D^{*+} \rightarrow D^0 \pi^+, D^0 \rightarrow K^- \pi^+$
τ_{SIG}	412.9 ± 3.8	408.9 ± 14.3	415.9 ± 7.6
S	1.08 ± 0.02	1.12 ± 0.07	1.00 ± 0.05
S_{tail}	3.43 ± 0.13	3.03 ± 0.26	2.56 ± 0.25
f_{tail}	0.042 ± 0.005	0.060 ± 0.017	0.109 ± 0.038
S_{BG}	1.15 ± 0.02	1.12 ± 0.03	$1.15(\text{fixed})$
τ_{BG}	428 ± 32	463 ± 37	$428(\text{fixed})$
$f_{\tau BG}$	0.13 ± 0.01	0.21 ± 0.02	$0.13(\text{fixed})$

(b) Fit parameters for the D^+ decay modes.

Fit parameters	$D^+ \rightarrow \phi \pi^+$	$D^{*+} \rightarrow D^+ \pi^0, D^+ \rightarrow K^- \pi^+ \pi^+$
τ_{SIG}	977^{+68}_{-62}	1038^{+25}_{-24}
S	0.7 ± 0.2	$0.73^{+0.11}_{-0.12}$
S_{tail}	3.2 ± 0.7	$1.79^{+0.21}_{-0.16}$
f_{tail}	0.05 ± 0.05	0.35 ± 0.11
S_{BG}	$1.16^{+0.08}_{-0.09}$	$0.88^{+0.11}_{-0.10}$
τ_{BG}	368^{+102}_{-79}	447^{+40}_{-40}
$f_{\tau BG}$	$0.29^{+0.09}_{-0.07}$	$0.52^{+0.05}_{-0.04}$

(c) Fit parameters for the D_s^+ decay modes.

Fit parameters	$D_s^+ \rightarrow \phi \pi^+$	$D_s^+ \rightarrow \bar{K}^{*0} K^+$
τ_{SIG}	468 ± 19	504^{+34}_{-33}
S	1.13 ± 0.07	0.98 ± 0.11
S_{tail}	$3.9^{+0.9}_{-0.6}$	$2.8^{+0.6}_{-0.4}$
f_{tail}	$0.05^{+0.03}_{-0.02}$	$0.07^{+0.04}_{-0.03}$
S_{BG}	$1.26^{+0.08}_{-0.07}$	1.20 ± 0.05
τ_{BG}	555^{+159}_{-118}	942^{+111}_{-98}
$f_{\tau BG}$	$0.19^{+0.08}_{-0.07}$	0.20 ± 0.03

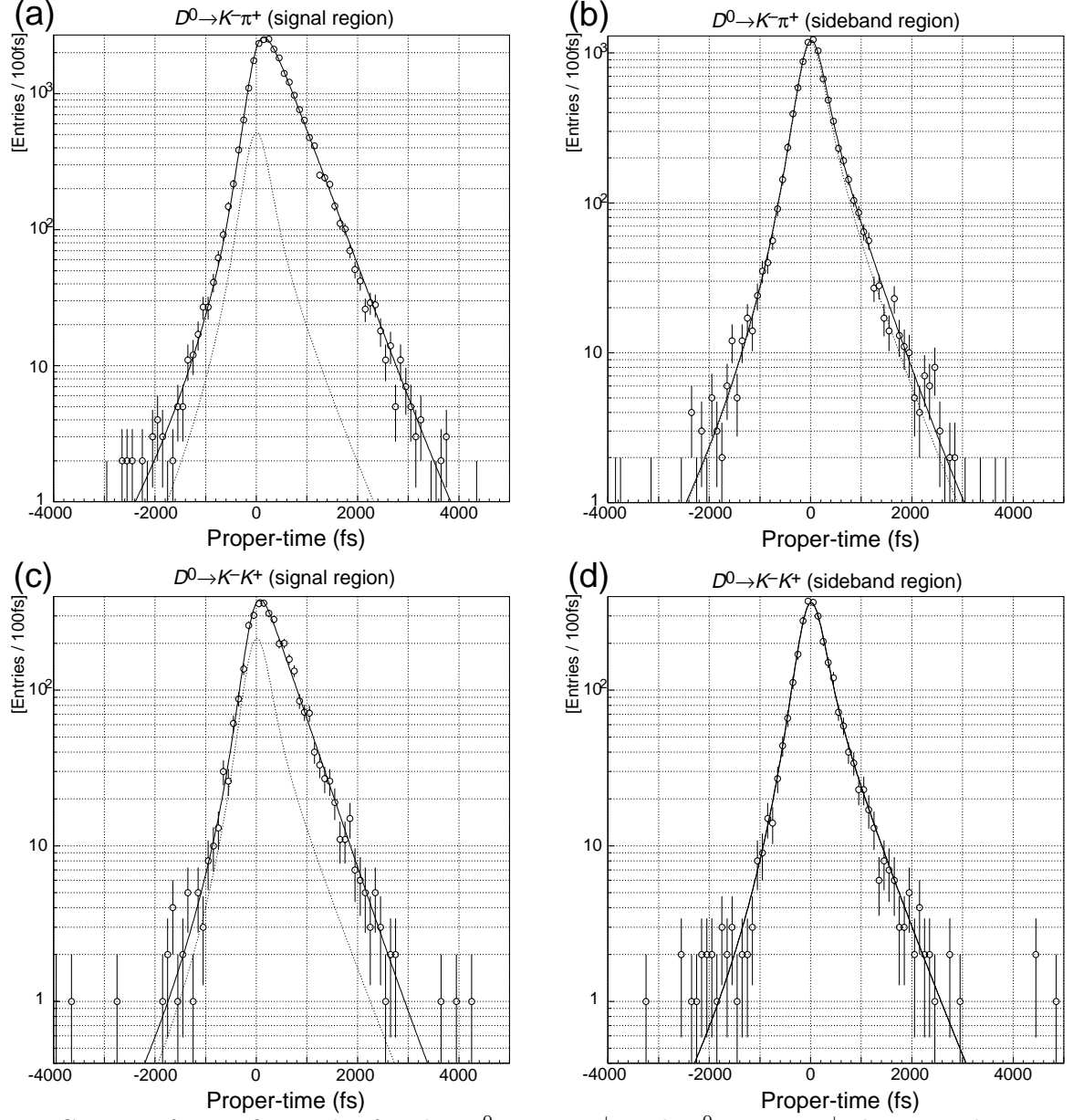


FIG. 12. Lifetime fit results for the $D^0 \rightarrow K^- \pi^+$ and $D^0 \rightarrow K^- K^+$ decay modes. Here (a) and (c) show the results in the D^0 mass signal region and (b) and (d) show the results in the D^0 mass sideband region.

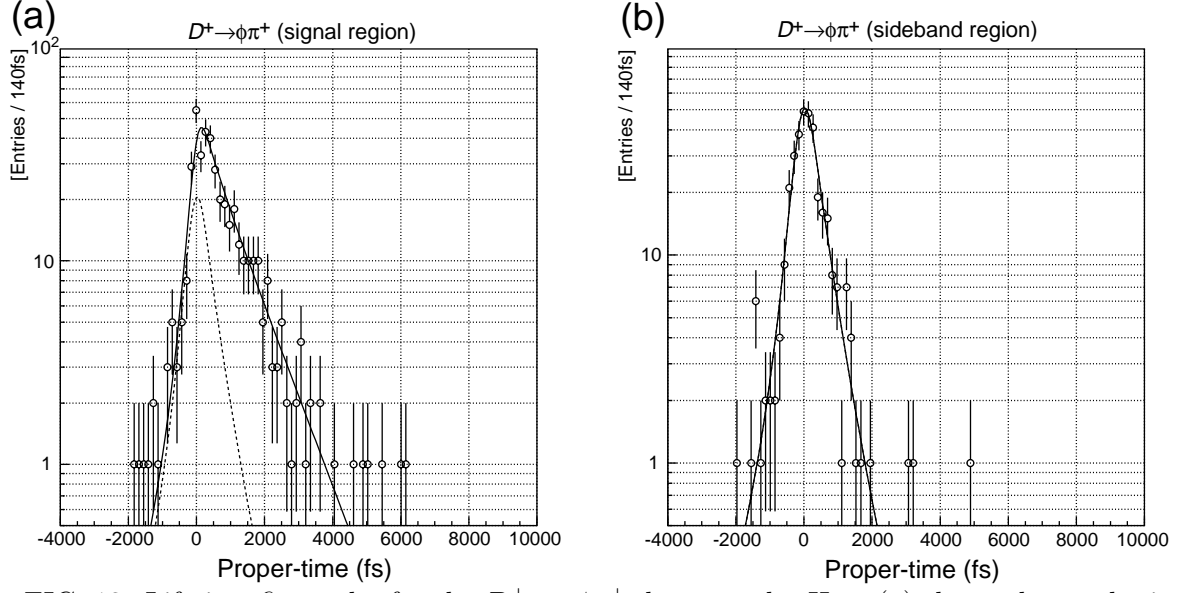


FIG. 13. Lifetime fit results for the $D^+ \rightarrow \phi\pi^+$ decay mode. Here (a) shows the results in the D^+ mass signal region and (b) shows the results in the D^+ mass sideband region.

TABLE VI. Summary of confidence levels of the fits derived from toy Monte Carlo experiments for each decay chain.

decay chain	C.L. of fit (%)
$D^0 \rightarrow K^-\pi^+$	3
$D^0 \rightarrow K^-K^+$	17
$D^{*+} \rightarrow D^0\pi^+, D^0 \rightarrow K^-\pi^+$	74
$D^+ \rightarrow \phi\pi^+$	17
$D^{*+} \rightarrow D^+\pi^0, D^+ \rightarrow K^-\pi^+\pi^+$	4
$D_s^+ \rightarrow \phi\pi^+$	33
$D_s^+ \rightarrow \bar{K}^{*0}K^+$	26

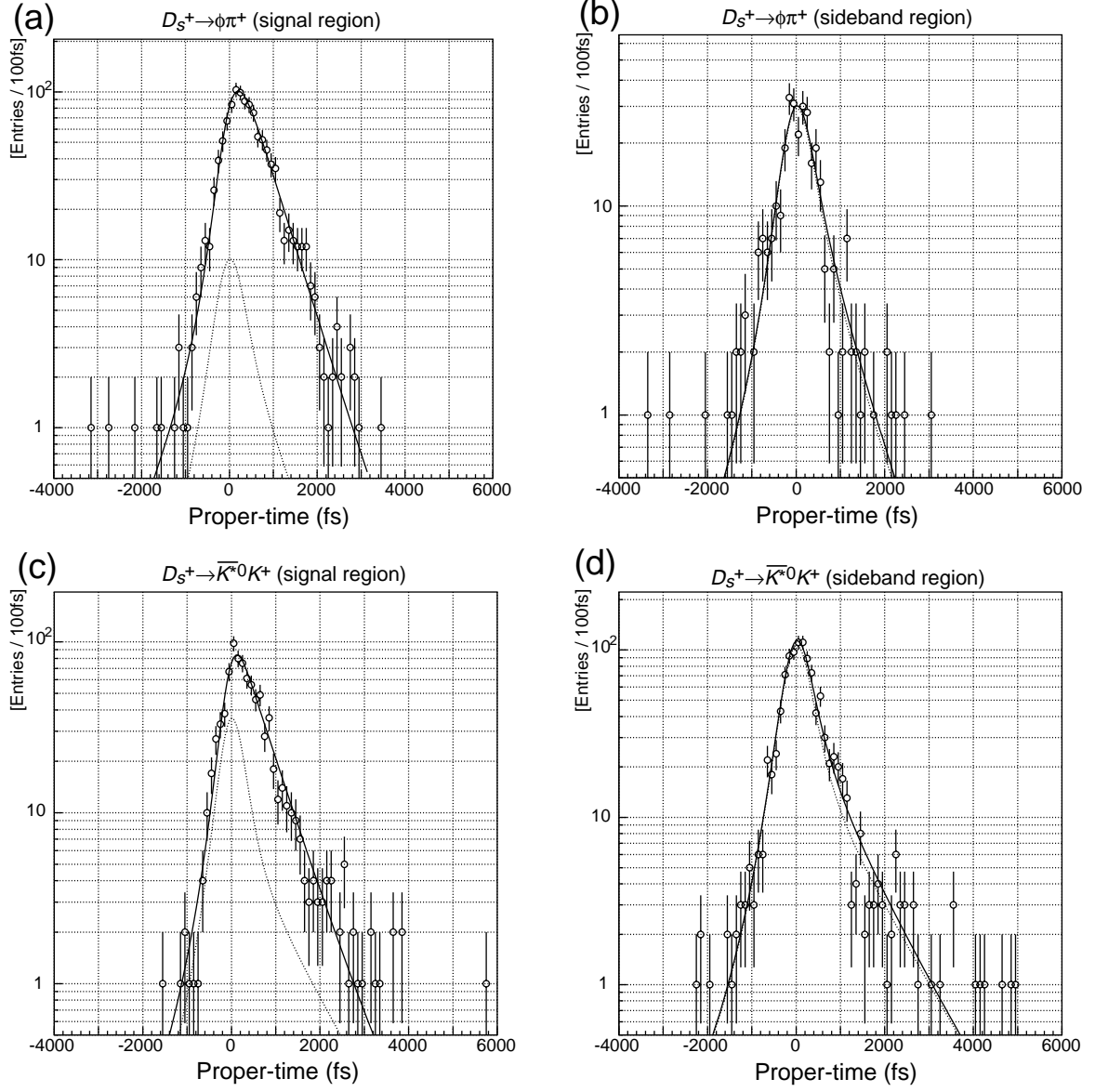


FIG. 14. Lifetime fit results for the $D_s^+ \rightarrow \phi \pi^+$ and $D_s^+ \rightarrow \bar{K}^{*0} K^+$ decay modes. Here (a) and (c) show the results in the D_s^+ mass signal region and (b) and (d) show the results in the D_s^+ mass sideband region.

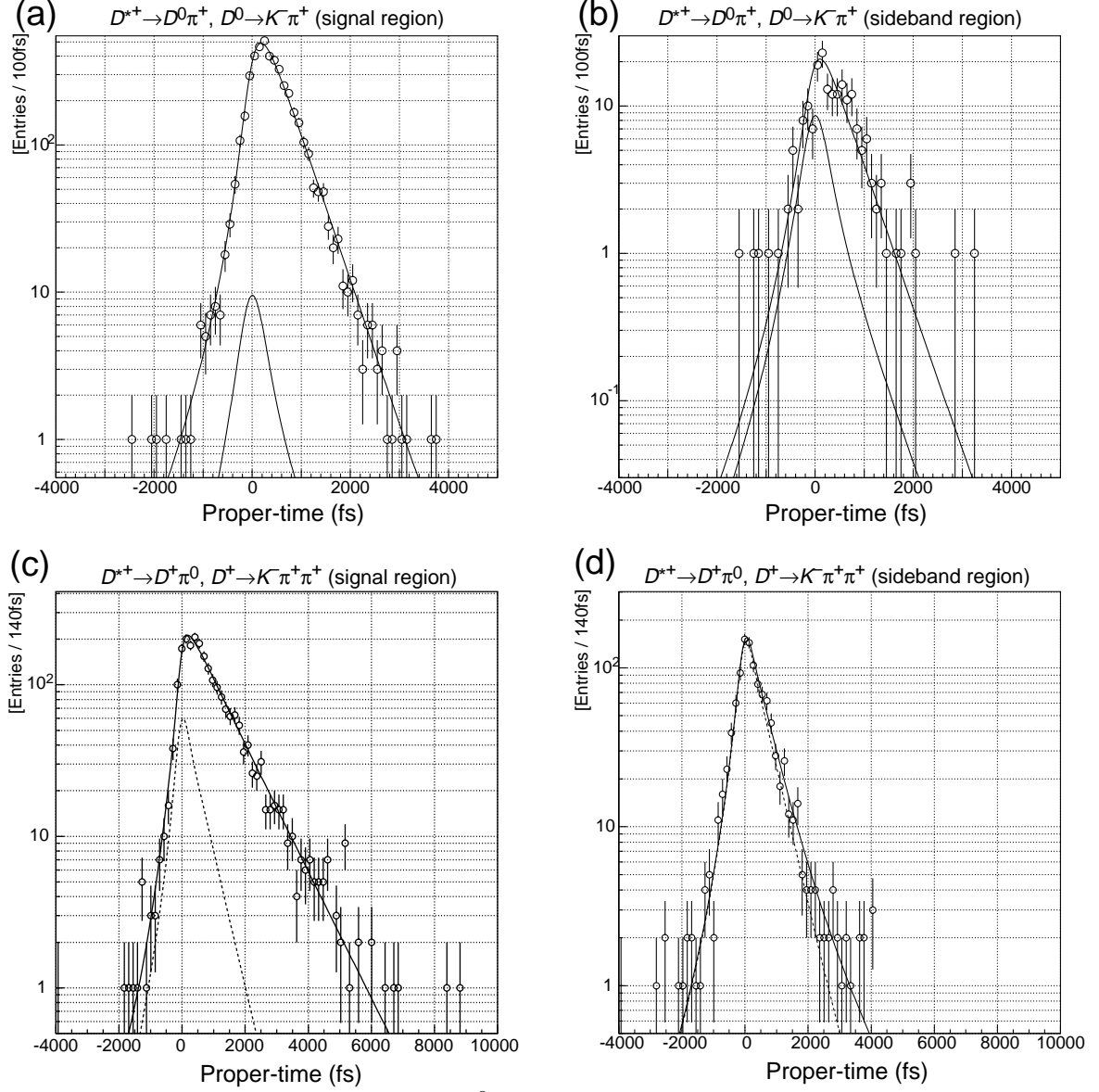


FIG. 15. Lifetime fit results for the $D^0 \rightarrow K^- \pi^+$ and $D^+ \rightarrow K^- \pi^+ \pi^+$ decay modes with D^* requirements. Here (a) and (c) show the results in the D -mass signal region and (b) and (d) show the results in the D -mass sideband region.

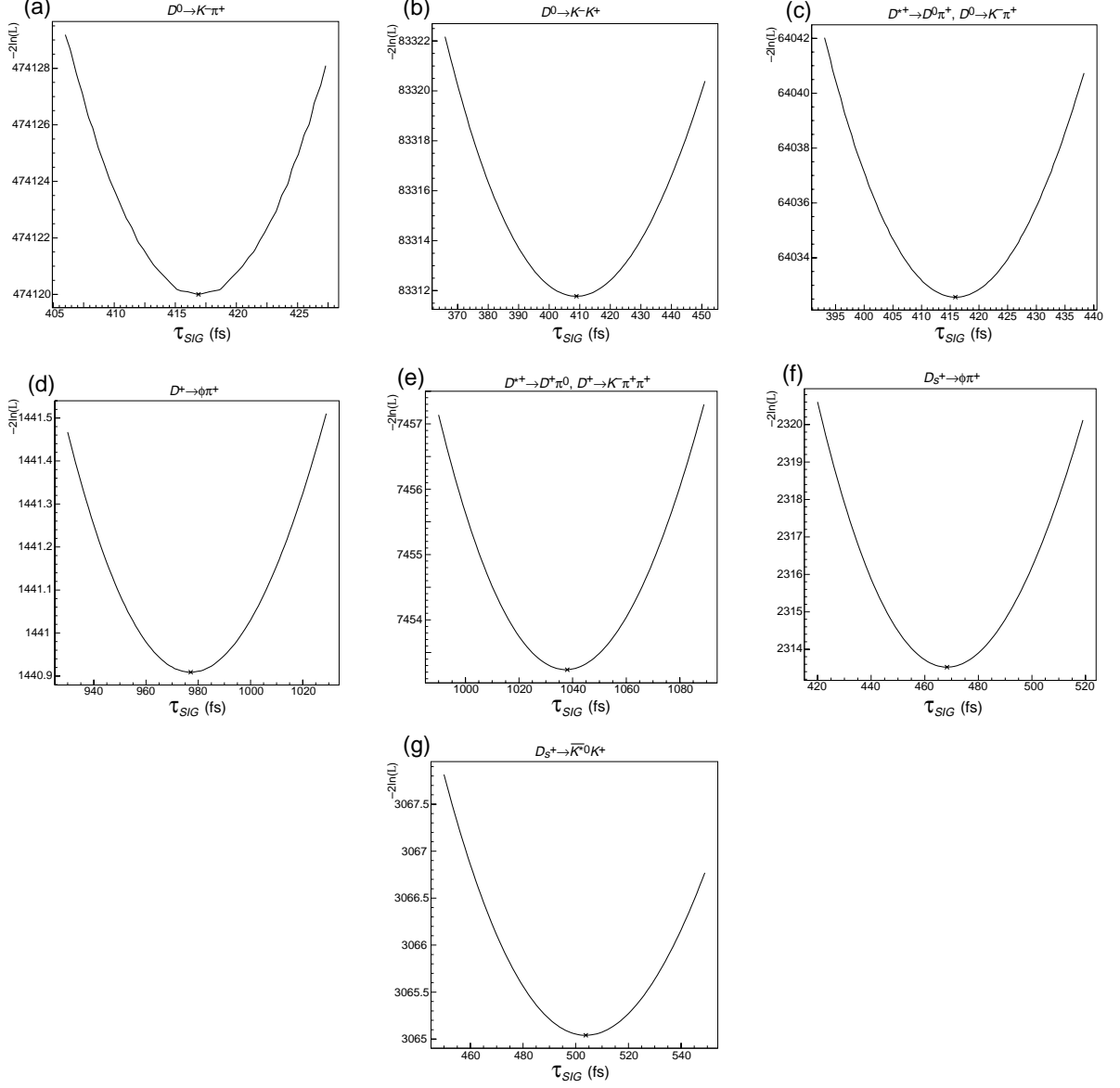


FIG. 16. The log-likelihood as a function of τ_{SIG} for the (a) $D^0 \rightarrow K^- \pi^+$, (b) $D^0 \rightarrow K^- K^+$, (c) $D^{*+} \rightarrow D^0 \pi^+$, $D^0 \rightarrow K^- \pi^+$, (d) $D^+ \rightarrow \phi \pi^+$, (e) $D^{*+} \rightarrow D^+ \pi^0$, $D^+ \rightarrow K^- \pi^+ \pi^+$, (f) $D_s^+ \rightarrow \phi \pi^+$ and (g) $D_s^+ \rightarrow \bar{K}^{*0} K^+$ decay modes.

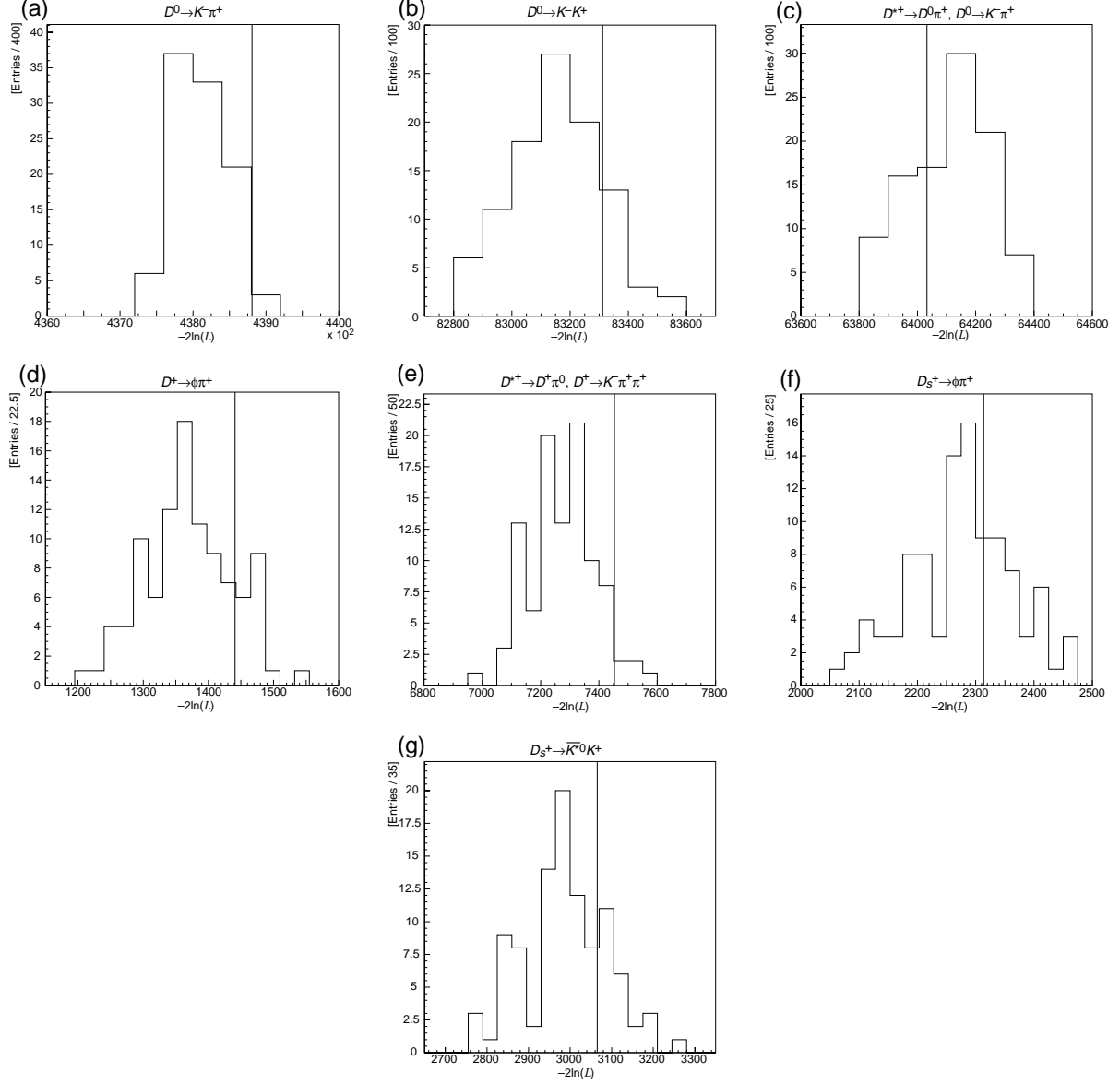


FIG. 17. The log-likelihood distribution from 100 toy Monte Carlo experiments for (a) $D^0 \rightarrow K^- \pi^+$, (b) $D^0 \rightarrow K^- K^+$, (c) $D^{*+} \rightarrow D^0 \pi^+, D^0 \rightarrow K^- \pi^+$, (d) $D^+ \rightarrow \phi \pi^+$, (e) $D^{*+} \rightarrow D^+ \pi^0, D^+ \rightarrow K^- \pi^+ \pi^+$, (f) $D_s^+ \rightarrow \phi \pi^+$ and (g) $D_s^+ \rightarrow \bar{K}^{*0} K^+$. Our fit results are indicated by vertical lines.

TABLE VII. Summary of systematic errors for each decay mode.

(a) Systematic errors for the D^0 decay modes.

Fit parameters	Systematic error		
	$D^0 \rightarrow K^- \pi^+$	$D^0 \rightarrow K^- K^+$	$D^0 \rightarrow K^- \pi^+ (D^{*+} \text{ tag})$
IP	$+0.2$ -0.3	$+1.3$ -0.4	± 0.4
Efficiency	± 1.8	± 1.8	± 3.6
Vertexing cuts	± 1.0	± 2.2	$+3.8$ -5.8
Decay vertex	± 1.9	± 1.8	± 2.0
Resolution function	$+1.5$ -1.7	$+3.4$ -3.6	$+0.1$ -0.4
Background	$+1.0$ -0.4	$+8.3$ -3.1	± 0.7
D -mass sideband region	$+0.0$ -0.6	$+0.0$ -1.1	$+0.0$ -2.0
Total	± 3.4	$+9.7$ -5.9	$+5.6$ -7.4

(b) Systematic errors for the D^+ decay modes.

Fit parameters	Systematic error	
	$D^+ \rightarrow \phi \pi^+$	$D^+ \rightarrow K^- \pi^+ \pi^+ (D^{*+} \text{ tag})$
IP	$+14$ -2	$+10$ -13
Efficiency	± 7	± 8
Vertexing cuts	$+2$ -0	$+7$ -3
Decay vertex	± 2	± 2
Resolution function	± 2	$+3$ -2
Background fraction	$+20$ -16	$+6$ -10
D -mass sideband region	$+2$ -0	$+1$ -2
Total	$+26$ -18	$+16$ -19

(c) Systematic errors for the D^+ decay modes.

Fit parameters	Systematic error	
	$D_s^+ \rightarrow \phi \pi^+$	$D_s^+ \rightarrow \bar{K}^{*0} K^+$
IP	$+1.0$ -1.6	$+1$ -4
Efficiency	± 2.1	± 3
Vertexing cuts	$+3.3$ -0.5	$+0$ -4
Decay vertex	± 2.0	± 2
Resolution function	± 1.9	± 4
Background fraction	$+1.5$ -2.8	$+5$ -8
D -mass sideband region	$+0.0$ -0.6	$+2$ -3
Total	$+5.1$ -7.0	$+8$ -12

efficiency at $t = 0$. The slopes are found to be $\alpha = (-14.1 \pm 5.5) \times 10^{-6} \text{ fs}^{-1}$ for the $D^0 \rightarrow K^- \pi^+$ mode, $\alpha = (1.5 \pm 3.6) \times 10^{-6} \text{ fs}^{-1}$ for the $D^+ \rightarrow K^- \pi^+ \pi^+$ mode and $\alpha = (-2.1 \pm 4.8) \times 10^{-6} \text{ fs}^{-1}$ for the $D_s^+ \rightarrow \phi \pi^+$ mode. A non-zero slope α corresponds to a bias of $\alpha\tau^2$ in the lifetime measurement. *

This effect has also been assessed by performing binned maximum likelihood fits on the true proper-time distributions for all generated events, and then on reconstructed events, with a pure exponential function. The difference of lifetime obtained from the two fits is considered to be due to the bias in the reconstruction efficiency. Fig 19 shows the true proper-time distribution of the reconstructed events, together with a fit to an exponential function, for each of the major modes. The results for all modes are summarized in Table VIII.

In the binned maximum likelihood fits, the χ^2 of the fit is computed using the formula [15]

$$\chi^2 = 2 \sum_i n_i \ln(n_i/y_i),$$

where n_i and y_i are the observed and expected numbers of events in the i th bin; the corresponding confidence levels are summarized in Table VIII. In each case the quality of the fit is found to be good.

Although the expected bias is within one standard deviation of zero in most modes, we find that the central value is consistently negative, *i.e.* the lifetime is, in general, underestimated. We have corrected for this bias based on the exponential fit method, and included the uncertainty on the bias as a systematic error.

TABLE VIII. Summary of expected biases in the lifetime measurement due to the reconstruction efficiency for each decay chain.

Modes	Linear fit method		Exponential fit method	
	expected bias (fs)	C.L. (%)	expected bias (fs)	C.L. (%)
$D^0 \rightarrow K^- \pi^+$	-2.4 ± 0.9	4	-1.9 ± 1.8	30
$D^0 \rightarrow K^- K^+$	-3.6 ± 1.3	48	-1.6 ± 1.8	30
$D^0 \rightarrow K^- \pi^+ (D^{*+} \text{ tag})$	-3.6 ± 1.8	39	-2.5 ± 3.6	57
$D^+ \rightarrow \phi \pi^+$	0 ± 7	89	3 ± 7	36
$D^+ \rightarrow K^- \pi^+ \pi^+$	1.6 ± 3.9	91	-11 ± 8	64
$D_s^+ \rightarrow \phi \pi^+$	-0.5 ± 1.1	67	-1.9 ± 2.1	19
$D_s^+ \rightarrow \bar{K}^{*0} K^+$	-2.7 ± 2.9	27	-0.9 ± 2.7	66

- Vertexing cut dependence: Possible systematic effects due to the fit quality cut for the D decay and production vertices have also been studied. The confidence level cut

*We estimate the effect of the slope α on the lifetime measurement as $e^{-\frac{t}{\tau}}(1 + \alpha t) \approx e^{-\frac{t}{\tau}} e^{\alpha t} = e^{-\frac{1-\alpha\tau}{\tau}t} \approx e^{-\frac{1}{\tau(1+\alpha\tau)}t}$.

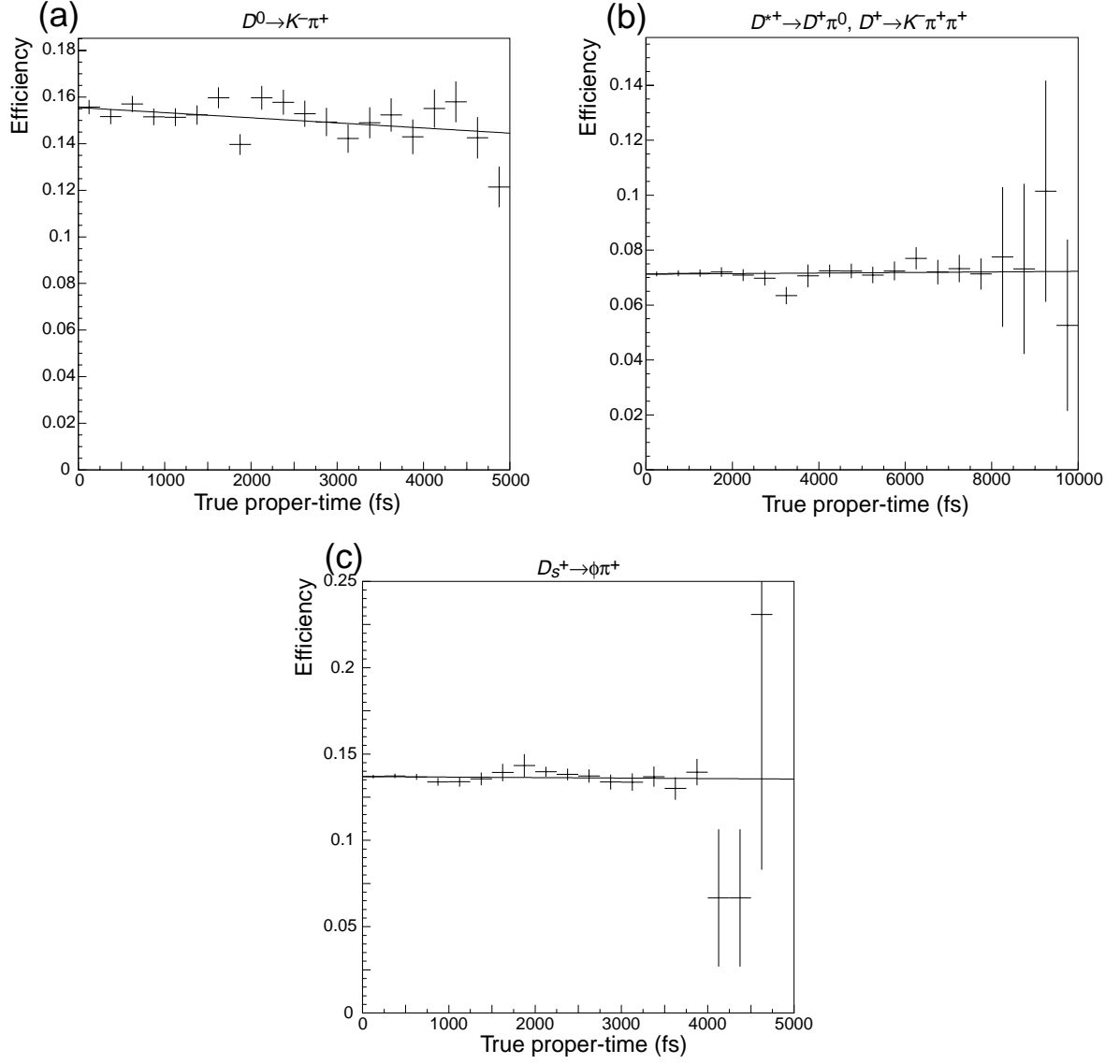


FIG. 18. The reconstruction efficiency as a function of the proper-time t for (a) $D^0 \rightarrow K^- \pi^+$, (b) $D^+ \rightarrow K^- \pi^+ \pi^+$ and (c) $D_s^+ \rightarrow \phi \pi^+$ from MC data.

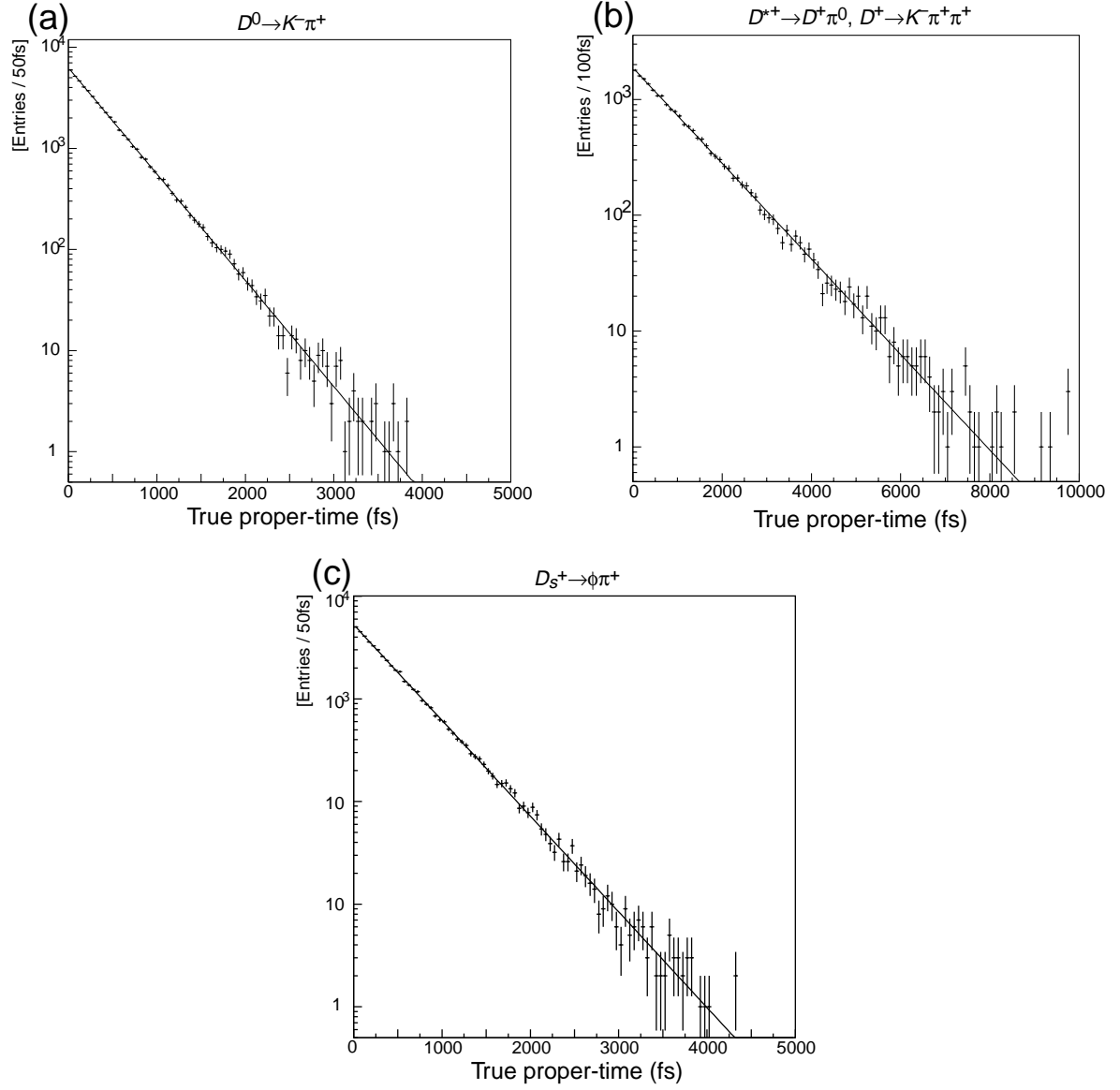


FIG. 19. The true proper-time distribution of reconstructed events, together with a fit to a pure exponential function for (a) $D^0 \rightarrow K^- \pi^+$, (b) $D^+ \rightarrow K^- \pi^+ \pi^+$ and (c) $D_s^+ \rightarrow \phi \pi^+$ from MC data.

for the vertex fit has been varied to estimate the systematic error associated with the estimation of fraction for badly measured events.

- Decay vertex: The possibility of a bias in the reconstruction of the decay vertex has been evaluated using a “zero-lifetime” sample: $\gamma\gamma \rightarrow \rho^0 \rho^0 \rightarrow \pi^+ \pi^- \pi^+ \pi^-$ events. Fig 20 shows the decay length distribution of ρ^0 candidates from $\gamma\gamma \rightarrow \rho^0 \rho^0 \rightarrow \pi^+ \pi^- \pi^+ \pi^-$ events: a fit to a sum of two Gaussian yields a mean value of $0.17 \pm 0.99 \mu\text{m}$ for the two-body analysis. For three-body decays, the combination which gives the largest momentum is chosen for each event. In this case, the mean value is found to be $0.09 \pm 1.06 \mu\text{m}$. Since the observed mean value is consistent with zero, we do not make any correction. We estimate the systematic error associated with a possible bias in the decay length reconstruction by adding a fixed value ($0.99 \mu\text{m}$ for two-body decay modes and $1.06 \mu\text{m}$ for three-body decay modes) to the reconstructed D decay length during the analysis.

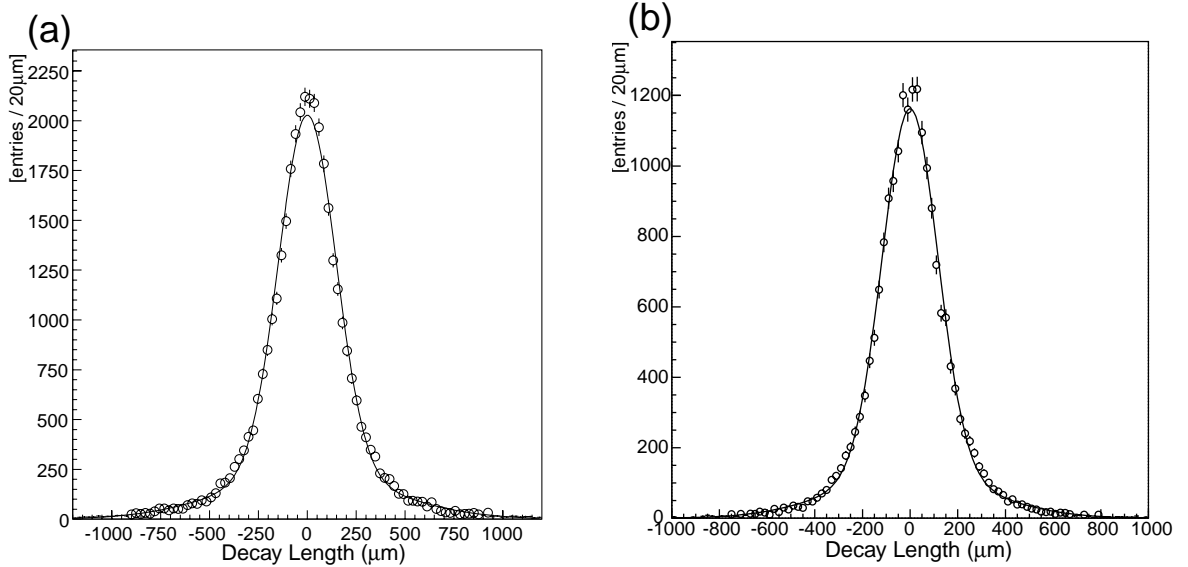


FIG. 20. The decay length distribution of the ρ^0 candidates from $\gamma\gamma \rightarrow \rho^0 \rho^0 \rightarrow \pi^+ \pi^- \pi^+ \pi^-$ events for (a) two-body analysis and (b) three-body analysis.

B. Systematic error due to fit

- Resolution function: The lifetime fit for each mode has been repeated with various changes to the resolution function, to provide an estimate of systematic errors associated with the choice of parameterization: the ratios S_{BG}/S and S_{tail}^{BG}/S_{tail} have been varied by the error obtained from MC data; a global resolution σ_{mis} has been used to represent the tail, instead of the event-by-event term $S_{tail} \cdot \sigma_t$; and the ratio of resolutions for the two background components (*i.e.* backgrounds with and without

lifetime) has been varied by $\pm 20\%$ from the default value of 1.0, to account for a possible difference in resolution.

- **Background fraction:** As described in section VI, the signal and background parts of the likelihood function are weighted by $f_{SIG}(M_D)$ and $(1 - f_{SIG}(M_D))$ respectively, where the “signal fraction” $f_{SIG}(M_D)$ is determined for each event based on a fit to the D -mass distribution in the data. The associated systematic error is estimated as follows: the $\pm 1\sigma$ values of f_{SIG} are calculated at all masses M_D , using the covariance matrix of the parameters of the D -mass fit; the $+1\sigma$ and the -1σ values are then used to perform two new fits for the D lifetime; the differences from the standard fit are taken as measures of the systematic error.

The background itself is divided into two components, one (a fraction $f_{\tau BG}$) with lifetime and one (a fraction $1 - f_{\tau BG}$) with zero lifetime; here, the parameter $f_{\tau BG}$ is allowed to float in the fit. This procedure has been tested by comparing the fitted value of $f_{\tau BG}$ in the Monte Carlo with the value obtained by fitting only the background events, using the background part of the likelihood function. The simultaneous fit of signal and background is found to bias the lifetime fraction $f_{\tau BG}$, returning a value 0.72 times the result of the background-only fit. To account for this effect, the fraction $f_{\tau BG}$ returned by each fit to the data has been scaled by $1/0.72$, and fixed in a new lifetime fit; any difference in the fitted D lifetime is then taken as a measure of the systematic error.

- **D -mass sideband region:** The parameters of the background are effectively determined by the contribution of events in the D -mass sideband to the fit. Some bias may therefore occur if the properties of the background vary with the D mass. The potential size of such an effect is estimated by varying the bounds of the D -mass sideband region, and repeating the fit. The ranges used are $-70 \sim -50$ MeV/ c^2 and $60 \sim 80$ MeV/ c^2 for the $D^0 \rightarrow K^-\pi^+$ analysis and $\pm 40 \sim \pm 60$ MeV/ c^2 for the remaining decay modes.

VIII. DETERMINATION OF LIFETIME RATIOS AND y_{CP}

We measure the D^0 meson lifetime to be $\tau(D^0) = (414.8 \pm 3.8 \pm 3.4)$ fs using the decay mode $D^0 \rightarrow K^-\pi^+$. The result from $D^0 \rightarrow K^-\pi^+$ with a D^{*+} tag is not combined with this value, as it is derived from the same data sample. However, since the D^{*+} tag eliminates backgrounds, it provides a useful consistency check: we find no significant difference between the two results.

The D^+ meson lifetime is measured to be (1049_{-24}^{+25+16}) fs for the $D^+ \rightarrow K^-\pi^+\pi^+$ decay sample and (974_{-62}^{+68+26}) fs for the $D^+ \rightarrow \phi\pi^+$ decay sample. Combining these results, we obtain $\tau(D^+) = (1040_{-22}^{+23} \pm 18)$ fs.

The D_s^+ meson lifetime is measured to be $(470 \pm 19_{-7}^{+5})$ fs for the $D_s^+ \rightarrow \phi\pi^+$ decay sample and (505_{-33}^{+34+8}) fs for the $D_s^+ \rightarrow \bar{K}^{*0}K^+$ decay sample. Combining these results we obtain $\tau(D_s^+) = (479_{-16}^{+17+6})$ fs. The $\phi \rightarrow K^+K^-$ decay in the $D_s^+ \rightarrow \phi\pi^+$ mode has a very small Q value, resulting in the kaons having nearly the same direction. Possible systematic effects associated with this kinematic feature are evaluated by the analysis of $D^+ \rightarrow \phi\pi^+$ and $D_s^+ \rightarrow \bar{K}^{*0}K^+$: in both cases, a lifetime consistent with, but larger than the corresponding

$D \rightarrow \phi\pi^+$ lifetime is obtained. Contrary to this trend, the $D \rightarrow \phi\pi$ decays in the Monte Carlo yield longer lifetime results within the statistical error (8 fs). We therefore conclude that there is no significant systematic effect due to the kinematics of $\phi \rightarrow K^+K^-$ decays.

Combining the D^0 , D^+ and D_s^+ lifetime measurements, we find the ratios of D^+ and D_s^+ lifetimes with respect to the D^0 lifetime to be $\tau(D^+)/\tau(D^0) = 2.51 \pm 0.06 \pm 0.04$ and $\tau(D_s^+)/\tau(D^0) = 1.15 \pm 0.04^{+0.01}_{-0.02}$. Comparing D^0 lifetimes through the $D^0 \rightarrow K^-\pi^+$ and $D^0 \rightarrow K^-K^+$ decays, we obtain an estimate of the lifetime difference of the two CP eigenstates, $y_{CP} = (1.0^{+3.8+1.1}_{-3.5-2.1})\%$. Under the assumption of Gaussian errors, this corresponds to a 95% confidence interval $-7.0\% < y_{CP} < 8.7\%$. We consider the correlations of systematic errors associated with the reconstruction and resolution functions. These correlations are properly taken into account when we combine two or more measurements *e.g.* in the case of y_{CP} .

Table IX compares our results with PDG99 world averages [16] and recent measurements by E791 [6,7], CLEO [5] and FOCUS [9,10].

TABLE IX. Comparison of our results with PDG99 world averages and recent measurements.

Experiment	$\tau(D^0)$ fs	$\tau(D^+)$ fs	$\tau(D_s^+)$ fs	y_{CP} %
PDG99	415 ± 4	1057 ± 15	495 ± 13	–
E791	$413 \pm 3 \pm 4$	–	$(518 \pm 14 \pm 7)^\dagger$	$0.8 \pm 2.9 \pm 1.0$
CLEO	$408.5 \pm 4.1^{+3.5}_{-3.4}$	$1034 \pm 22^{+10}_{-13}$	$486 \pm 15 \pm 5$	–
FOCUS	$409.2 \pm 1.3^\ddagger$	–	$506 \pm 8^\ddagger$	$3.42 \pm 1.39 \pm 0.74$
Belle	$414.8 \pm 3.8 \pm 3.4$	$1040^{+23}_{-22} \pm 18$	479^{+17+6}_{-16-8}	$1.0^{+3.8+1.1}_{-3.5-2.1}$

[†]This result is included in the PDG99 world average.

[‡]No systematic error is given.

IX. CONCLUSIONS

We present new measurements of charmed meson lifetimes using a data sample of 2.75 fb^{-1} of e^+e^- collisions, collected with the Belle detector near the $\Upsilon(4S)$. Unbinned maximum likelihood fits to proper-time distributions of fully reconstructed charmed meson candidates yield the following results for the lifetimes and their ratios:

$$\begin{aligned}
\tau(D^0) &= (414.8 \pm 3.8 \pm 3.4) \text{ fs}, \\
\tau(D^+) &= (1040^{+23}_{-22} \pm 18) \text{ fs}, \\
\tau(D_s^+) &= (479^{+17+6}_{-16-8}) \text{ fs}, \\
\tau(D^+)/\tau(D^0) &= 2.51 \pm 0.06 \pm 0.04, \\
\tau(D_s^+)/\tau(D^0) &= 1.15 \pm 0.04^{+0.01}_{-0.02}.
\end{aligned}$$

In addition, we have measured the lifetime difference between the two CP eigenstates of the D^0 meson to be

$$y_{CP} = (1.0^{+3.8+1.1}_{-3.5-2.1})\%,$$

corresponding to a 95% confidence interval,

$$-7.0\% < y_{CP} < 8.7\%.$$

The statistical uncertainties on the lifetimes are already comparable to those of the best published measurements. Our studies of systematic effects are still preliminary.

X. ACKNOWLEDGMENT

We gratefully acknowledge the efforts of the KEKB group in providing us with excellent luminosity and running conditions and the help with our computing and network systems provided by members of the KEK computing research center. We thank the staffs of KEK and collaborating institutions for their contributions to this work, and acknowledge support from the Ministry of Education, Science, Sports and Culture of Japan and the Japan Society for the Promotion of Science; the Australian Research Council and the Australian Department of Industry, Science and Resources; the Department of Science and Technology of India; the BK21 program of the Ministry of Education of Korea and the Basic Science program of the Korea Science and Engineering Foundation; the Polish State Committee for Scientific Research under contract No.2P03B 17017; the Ministry of Science and Technology of Russian Federation; the National Science Council and the Ministry of Education of Taiwan; the Japan-Taiwan Cooperative Program of the Interchange Association; and the U.S. Department of Energy.

REFERENCES

- [1] G. Bellini, I.I. Bigi and P.J. Dornan, Phys. Rep. **289** (1997) 1.
- [2] J. R. Raab *et al.* (E691) Phys. Rev. **D37** (1988) 2391.
- [3] P. L. Frabetti *et al.* (E687) Phys. Lett. **B323** (1994) 459.
- [4] P. L. Frabetti *et al.* (E687) Phys. Rev. Lett. **71** (1993) 827.
- [5] G. Bonvicini *et al.* (CLEO) Phys. Rev. Lett. 8245861999.
- [6] E.M. Aitala *et al.* (E791) Phys. Lett. B **445** (1999) 449.
- [7] E.M. Aitala *et al.* (E791) Phys. Rev. Lett. 83321999.
- [8] I.I. Bigi and N.G. Uraltsev, Z. Phys. C **62** (1994) 623.
- [9] J.M. Link *et al.* (FOCUS) hep-xp/0004034.
- [10] H.W.K. Cheung, “Review of Charm Lifetimes”, hep-ex/9912021.
- [11] R. Godang *et al.* (CLEO) hep-ex/0001060.
- [12] S. Bergmann, Y. Grossman, Z. Ligeti, Y. Nir and A.A. Petrov, hep-ph/0005181.
- [13] “KEKB B-Factory Design Report”, KEK Report 95-7(1995). K. Akai *et al.* “COMMISSIONING OF THE KEKB B-FACTORY”, Proc. Intl. Workshop on e+e- Factories, Sept. 21-24, 1999, KEK, Tsukuba, Japan, edited by K. Akai and E. Kikutani.(1999). H. Fukuma *et al.* “OBSERVATION OF VERTICAL BEAM BLOW-UP IN KEKB LOW ENERGY RING”, Proc. 2000 European Particle Accelerator Conference, Vienna(2000). Y. Funakoshi *et al.* “KEKB PERFORMANCE”, Proc. 2000 European Particle Accelerator Conference, Vienna(2000).
- [14] (SVD) G. Alimonti *et al.* “The Belle silicon vertex detector”, KEK preprint 2000-34.
 (CDC) H. Hirano *et al.* KEK Preprint 2000-2. M. Akatsu *et al.* DPNU-00-06.
 (ACC) T. Iijima *et al.* “Aerogel Cherenkov counter for the Belle detector”, Proceedings of the 7th International Conference on Instrumentation for Colliding Beam Physics, Hamamatsu, Japan, Nov. 15-19, 1999.
 (ECL) K. Ikeda *et al.* Nucl. Instrum. and Meth. **441** (2000) 401.
- [15] S. Baker and R.D. Cousins, Nucl. Instrum. and Meth. **221** (1984) 437.
- [16] C. Caso *et al.* The Eur. Phys. J. **C3** (1998) 1 and 1999 off-year partial update for the 2000 edition available on the PDG WWW pages (URL: <http://pdg.lbl.gov/>).